

# **Archive Mining for Kinematic Lensing in Galaxy Clusters**

A Thesis Presented

by

**Jiyun Di**

to

The Graduate School

in Partial Fulfillment of the Requirements

for the Degree of

**Master of Arts**

in

**Physics**

Stony Brook University

May 2024

**Stony Brook University**

The Graduate School

**Jiyun Di**

We, the thesis committee for the above candidate for the Master of Arts degree, hereby recommend acceptance of this thesis.

Anja von der Linden – Thesis Advisor  
Associate Professor, Department of Physics and Astronomy

Simon Birrer – Chairperson of Defense  
Assistant Professor, Department of Physics and Astronomy

Phil Armitage  
Professor, Department of Physics and Astronomy

This thesis is accepted by the Graduate School.

Celia Marshik  
Dean of the Graduate School

Abstract of the Thesis

# **Archive Mining for Kinematic Lensing in Galaxy Clusters**

by

**Jiyun Di**

**Master of Arts**

in

**Physics**

Stony Brook University

2024

Traditional measurement of weak lensing shear introduces a shape noise of  $\sim 0.26$ . Kinematic Lensing (KL) is a new technique using Tully-Fisher relation and multi-object spectroscopy with slits, to break the degeneracy between intrinsic shape and weak-lensing shear and reduce the resultant shape noise to  $\sim 0.04$ . This paper mines and reduces archived slit-spectroscopic data on the galaxy cluster sample investigated in the *Weighing the Giants* project. A total of 6 clusters with 17 masks and Keck/DEIMOS data are chosen which span a redshift range of  $z_{\text{Cl}} = 0.224\text{--}0.375$ , yielding 1138 spectra for 1120 galaxy targets in cluster fields. This study produces 443 secure redshifts and identifies 149 rotation curves, where 105 curves are from background source galaxies. The clusters and rotation curves are valuable databases contributing to a pilot KL study.

# Contents

<b>List of Figures</b>	<b>v</b>
<b>List of Tables</b>	<b>vi</b>
<b>Acknowledgments</b>	<b>vii</b>
<b>1 Introduction</b>	<b>1</b>
1.1 Galaxy Clusters . . . . .	1
1.1.1 Background . . . . .	1
1.1.2 Cluster Surveys . . . . .	2
1.2 Weak Lensing . . . . .	2
1.2.1 Weak Lensing Cosmology . . . . .	3
1.2.2 Shape Noise . . . . .	4
1.3 Kinematic Lensing . . . . .	5
1.3.1 Rotation Curves . . . . .	6
1.3.2 Tully-Fisher Rotational Speed . . . . .	8
1.3.3 Expectations of Kinematic Lensing . . . . .	8
<b>2 Kinematic Lensing on “Weighing the Giants” Galaxy Clusters</b>	<b>10</b>
2.1 Target Selection . . . . .	10
2.2 Data Reduction . . . . .	12
2.2.1 Keck/DEIMOS . . . . .	12
2.2.2 Raw and Calibration Data . . . . .	12
2.2.3 PypeIt: A Reduction Pipeline . . . . .	13
2.3 Results . . . . .	16
2.3.1 Spectroscopic Redshifts . . . . .	16
2.3.2 Rotation Curves and Velocity Fields . . . . .	19
2.4 Discussions and Future Works . . . . .	22
2.4.1 Redshift Pipeline . . . . .	22
2.4.2 Shear Measurement . . . . .	23
2.4.3 Future MOS Instruments . . . . .	23
2.4.4 Discoveries of Active Galactic Nucleus . . . . .	24
2.5 Conclusions . . . . .	24
<b>Bibliography</b>	<b>25</b>

# List of Figures

1.1	Similar observed galaxy shapes but from the lensed versus the oriented regimes . . . . .	4
1.2	Multi-object spectrograph (MOS) and 2D spectra on CCD . . . . .	5
1.3	Velocity field when inclination angle $i = 30^\circ$ and slit angle $\phi = 45^\circ$ . . . . .	7
1.4	Rotation curves by a slit . . . . .	7
2.1	Raw and calibration images of A2552 . . . . .	13
2.2	Neon-lamp spectrum and wavelength calibration . . . . .	14
2.3	Sky line subtraction . . . . .	15
2.4	Blended [O II] doublet lines . . . . .	18
2.5	Distribution of slit positions and non-duplicated secure redshifts of A2261 . . . . .	19
2.6	1D and 2D spectra with rotation curves . . . . .	20
2.7	Rotation curve fitting . . . . .	21
2.8	FIREFLY output . . . . .	23

# List of Tables

2.1	Clusters Observed from Keck/DEIMOS and Rotation Curves . . . . .	11
2.2	Keck/DEIMOS Characteristics . . . . .	12
2.3	Spectral Templates For Cross-Correlation . . . . .	17
2.4	Redshift Table of A2552 . . . . .	18

# Acknowledgments

*My deepest appreciation to my parents, Yuling Chen and Liang Di, for at least 25 years of financial and psychological support. Without a doubt, they represent the most wisdom and broadest perspectives of Chinese parents.*

*I thank Stony Brook University's Department of Physics and Astronomy for admitting me in 2022 for a 2-year master's degree. After the COVID-19 impact, transferring from an undergraduate senior to a normal employee in the industry was a tragedy for non-U.S. citizens with a science major, thus making U.S. astronomy/physics graduate schools so highly competitive<sup>1</sup> that I was not accepted by any of the 11 Ph.D. programs in U.S. graduate schools to which I applied. Stony Brook University saved my life with this in mind.*

*I express my sincerest gratitude to my undergraduate research supervisor at U of Arizona, Prof. Eiichi Egami, for providing academic guidance, arranging meetings (30+ discussions per year), reviewing paper drafts, and working on arXiv pre-prints and ApJ journal papers.*

*I extend my warmest thanks to my graduate research supervisor at Stony Brook University, Prof. Anja von der Linden. She spent both on-campus and online meeting sessions on making remarkable improvements in research, organizing academic planning in the first semester, and enhancing my data reduction skills.*

---

I am also thankful to Prof. Phil Armitage, Prof. Shufang Su, and Mr. Shawn Jackson for their precious recommendation for both my master's and Ph.D. application processes.

Since 2018, Tianyu Jiao has been my brother-in-arms. We've kept our friendships firm for years, even though we are usually separated in different locations. For references of young students who are reading this thesis, the reason for keeping this friendship is that we both often play the same and relevant video games, which brings a lot of happiness in common and necessary entertainment after studying hours.

I appreciate the cooperation of Anja von der Linden's Spectroscopy Team, including Alden Beck and Aaron Burke, and collaboration from U of Arizona, such as Prof. Tim Eifler, Prof. Elisabeth Krause, and Pranjal R. Singh.

---

<sup>1</sup>Porter, A. and Mulvey, P. (2022) "Postgraduation Planning During a Pandemic: Effects of COVID-19 on Physics and Astronomy Seniors' Career Paths", American Institute of Physics, 27 Oct. Available at: <https://www.aip.org/statistics/postgraduation-planning-during-a-pandemic-effects-of-covid-19-on-physics-and-astronomy-seniors-career-paths> (Accessed 4 Mar 2024).

I thank my fellow students such as Haowei Zheng, Canyu Zhang, Ben Levine, Qi'an Yu, Xiangyu Huang, Dr. Fengwu Sun, Dr. Yujing Qin, Zhuo Lyu, and Kai-Chun Lee. My colleagues, such as Fan Chen, Xiaohan Fei, and Zehao Dong, also deserve my gratitude. They gave me their care and valuable advice on aspects of astronomy and industry. Without you all, I wouldn't have achieved success today.

I also deeply appreciate the best wishes from my high school and middle school classmates and astronomy club members: Rangsen Wu, Chenhan Guo, Jian Xiao, Xu Yang, Haochen Qi, Guanghao He, Huaijian Wang, Pengpei Zhu, Gepeng Ding, Xiaorui Lu, Jiaxuan Li, and others. During the pandemic, they kept in touch with me and sent their best wishes that I could accomplish my goal of proceeding with astronomical studies lifetime.

---

During my years of studying abroad in the United States, I have gained a deeper understanding of astronomy and astrophysics in academia and industry. During this time, I have experienced disappointment, complacency, regret, and helplessness. More and more negative emotions have instead led me to think calmly. I am constantly summarizing what I have learned each year that can be used to better understand society. These are all worth remembering for me.

In only one moment, one can fall into the abyss, deteriorate, and be overwhelmed. I encountered a severe mental disorder from July 2022 to September 2022, struggling with my future and feeling depressed after the failure of applying to graduate schools. Fortunately, I am still accompanied by my parents, the best roommates and classmates, the faith in my spiritual world that others cannot understand, and the gaze of my passed-away middle school teacher in heaven. Thus, I was able to survive, happy, and free. My past life seemed to be naive, ideal, and prayerful; now my life was challenging but purposeful and full of a better future. I believe, and I do.

# Chapter 1

## Introduction

### 1.1 Galaxy Clusters

#### 1.1.1 Background

Clusters of galaxies are large gravitationally-bound structures in the Universe. Typically, galaxy clusters are located at the crossings of large-scale structure webs and extend to a radius of a few Mpc physically. A galaxy cluster contains hundreds to thousands of galaxies and encloses a typical mass of  $10^{14} - 10^{15} \text{ M}_\odot$  (e.g., [Zwicky 1937](#)). To date, the most massive galaxy clusters at an intermediate redshift range of  $z \sim 0.1 - 1$  have masses between  $1$  and  $3.2 \times 10^{15} \text{ M}_\odot$  and the most distant cluster is at  $z \sim 2.5$  with a mass of  $\sim 10^{14} \text{ M}_\odot$  (e.g., [Jee et al. 2014](#), [Diego et al. 2020, 2023](#), [Wang et al. 2016](#)).

Galaxy clusters are important laboratories for cosmology. For example, the properties of galaxy clusters throughout the Universe's expansion history can provide significant insights on such a large scale. In terms of mass composition, a galaxy cluster consists of stars ( $\sim 1 - 3\%$ ), hot gas and plasma within the cluster core ( $\sim 15\%$ ), and cold dark matter ( $\sim 80\%$ ) ([Allen et al. 2011](#)). About 90 years ago, [Zwicky \(1933\)](#) found that the Coma cluster has  $\sim 400$  times greater mass density (obtained from galaxy velocity dispersion) than that calculated from the luminous component of the cluster. This cluster study first pointed out the presence of dark matter living inside the galaxy cluster. Follow-up studies confirmed the existence of dark matter by the detection of X-ray signals from the intracluster medium near the Coma cluster center (ICM; see [Kravtsov & Borgani 2012](#), for a review).

### 1.1.2 Cluster Surveys

Galaxy clusters can be identified across a variety of wavelengths. The optical and X-ray surveys have the longest histories. Half a century ago, [Abell \(1958\)](#) conducted the first cluster survey in the optical waveband and finally composed the Abell cluster catalog, which includes more than 4000 galaxy clusters.

In the **optical and near-infrared (near-IR)**, galaxy clusters are traditionally identified as over-densities of evolved red galaxies at similar redshifts. Many new approaches are utilized for cluster surveys, such as the CAMIRA algorithm which is applied to the HSC Subaru Strategic Program ([Oguri 2014](#), [Oguri et al. 2018](#), [Aihara et al. 2018](#)). Near-IR space telescopes extend the reach of optical surveys to redshifts  $z > 1$ .

In the **X-ray**, the central region of the galaxy cluster shows up as an extended emission source. The intracluster gas is nearly in hydrostatic equilibrium due to the cluster's deep gravitational potential, with a high virial temperature of  $10^7 - 10^8$  K and an energy of a few keVs. As electrons in the ICM plasma emit strong bremsstrahlung radiation, X-ray emission can show peaks, tracing the cluster's brightest central galaxies (BCGs) and indicating more trustful BCG identifications than optical surveys. X-ray surveys, such as the Massive Cluster Survey (MACS; [Ebeling et al. 2001, 2007, 2010](#)), the *ROSAT*-ESO Flux Limited X-ray (REFLEX; [Böhringer et al. 2004](#)), and the *ROSAT* Brightest Cluster Survey (BCS; [Ebeling et al. 1998, 2000](#)), offer crucial information on the cluster-scale environment, however, may be biased by the projection effects.

In the **millimeter-wave**, when a cosmic microwave background (CMB) photon passes through the ICM, the high-energy electron can inversely Compton-scatter the CMB photon (at  $T_{\text{CMB}} = 2.73$  K or  $\nu_{\text{CMB}} = 160$  GHz by Wien's Law), boosting to higher photon energy ( $\sim 400$  GHz). This boosting effect in the CMB observation, proposed by [Sunyaev & Zeldovich \(SZ, 1972\)](#), is known as the SZ Effect. The entire CMB specific intensity is blueshifted, resulting in a higher peak frequency at  $\sim 400$  GHz ([Carlstrom et al. 2002](#)). In the last decade, large radio telescopes such as the Atacama Cosmology Telescope and South Pole Telescope have been commissioned, making a bloom of the SZ-effect-selected galaxy cluster surveys (e.g., [Hasselfield et al. 2013](#), [Reichardt et al. 2013](#), [Bleem et al. 2015](#)).

## 1.2 Weak Lensing

According to General Relativity, a massive gravitational system can bend light, magnifying its background like a lens. Such a system usually consists of a galaxy cluster, a massive galaxy, and(or) a massive compact halo object (MACHO). This gravitational lensing effect changes the

image and shape of the background object (“source”), resulting in three types of lensing — strong lensing, weak lensing, and microlensing. The difference between strong and weak lensing is whether the source is strongly or weakly distorted, respectively. Strong lensing may have multiple, arc-like, and point-symmetric images, while weak lensing slightly changes the shapes and ellipticities of the source.

Weak lensing distortion includes the magnification/convergence ( $\kappa$ ), weak shear, and rotation effects on the intrinsic image. The weak shear mathematically describes the magnitude and direction of lensing by constructing a complex number

$$\gamma = \gamma_+ + i\gamma_\times, \quad (1.1)$$

where  $+$  means the component aligned with the major axis of the galaxy and  $\times$  is the component rotated by  $45^\circ$  relative to  $+$ . The ellipticities of the galaxy can be expressed as a complex number:  $\epsilon = \epsilon_+ + i\epsilon_\times$ . Therefore, the intrinsic shape/ellipticity ( $\epsilon_{\text{int}}$ ) turns into the observed shape/ellipticity ( $\epsilon_{\text{obs}}$ ) by<sup>1</sup>

$$\epsilon_{\text{obs}} = \gamma + \epsilon_{\text{int}}. \quad (1.2)$$

### 1.2.1 Weak Lensing Cosmology

Weak shears, ellipticities, and redshifts can statistically build up the shear maps and correlation functions that provide good probes for testing theoretical models of cosmology.

For instance, the convergence field ( $\kappa$ ) traces the projected gravitational potential along the line of sight out to some redshift. Weak-lensing mass maps can be inferred since weak lensing directly measures the total projected matter, including the dark matter, without tracing the baryonic components. The weak lensing mass estimation requires the following observables: the weak shear, the redshifts of the lensed galaxies, and assumptions on the mass profile of the cluster (see [Mandelbaum 2018](#), for a review).

The statistical shear–shear correlation function, known as cosmic shear, averages the product of ellipticities of galaxies in pairs and within redshift bins. In the complex Fourier-transformed space, the shear correlation gives shear power spectra as a function of the angular distance of pair-galaxies that are sensitive to assumed cosmology (see [Kilbinger 2015](#), for a review).

There are several methods of constraining cosmological parameters, such as using the weak-lensing observable covariance matrix, the likelihood function of observed data given a model with

---

<sup>1</sup>The equal sign here is an approximation referred from Equation (3.2) Case 1 of [Seitz & Schneider \(1997\)](#) in a weak lensing regime that satisfies  $\gamma^* \epsilon_{\text{int}} \ll 1$ , where  $\gamma^*$  is the complex conjugation of  $\gamma$ .

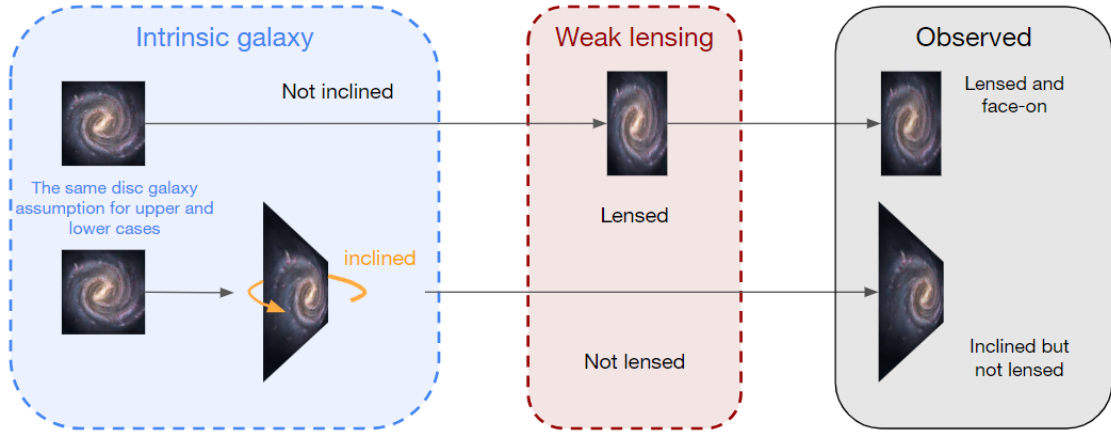


Figure 1.1: An example scheme of similar observed galaxy shapes from different regimes: the lensed (*in upper panel*) versus the oriented regimes (*in lower panel*).

a set of parameters (Kilbinger 2015), the intrinsic alignment of galaxy shapes without lensing effects, and the baryonic feedback effects in the case of small-scale cosmic shear (Xu et al. 2023).

### 1.2.2 Shape Noise

In an unlensed regime, the orientations of source galaxies are usually random, making galaxies intrinsically elliptical. It is difficult to determine whether the observed galaxy shape is due to an inclination angle along the light of sight, or whether the source galaxy is weakly-lensed, as illustrated in Figure 1.1. von der Linden et al. (2014a) point out that assuming the intrinsic ellipticities of galaxies are uniformly distributed in the cluster field is challenging. **The shear signal is very small ( $\sim 10^{-3}$ ), one order of magnitude smaller than the intrinsic ellipticity** (Huff et al. 2013, Pranjal et al. 2023). To measure the shear statistically, it is traditional to average the shapes of galaxies, assuming  $\langle \epsilon_{\text{int}} \rangle = 0$ , and taking the average of Equation 1.2:

$$\gamma = \langle \epsilon_{\text{obs}} \rangle. \quad (1.3)$$

Unfortunately, this “**shape noise**” can as high as  $\sigma_\epsilon = \langle \epsilon_{\text{int}} \rangle \sim 0.26$  (Chang et al. 2013), on average per ellipticity component (either + or  $\times$  component) in the regime of random intrinsic orientations and ellipticities. The main goal of this thesis is to mitigate this shape noise using the following proposed method — Kinematic Lensing.

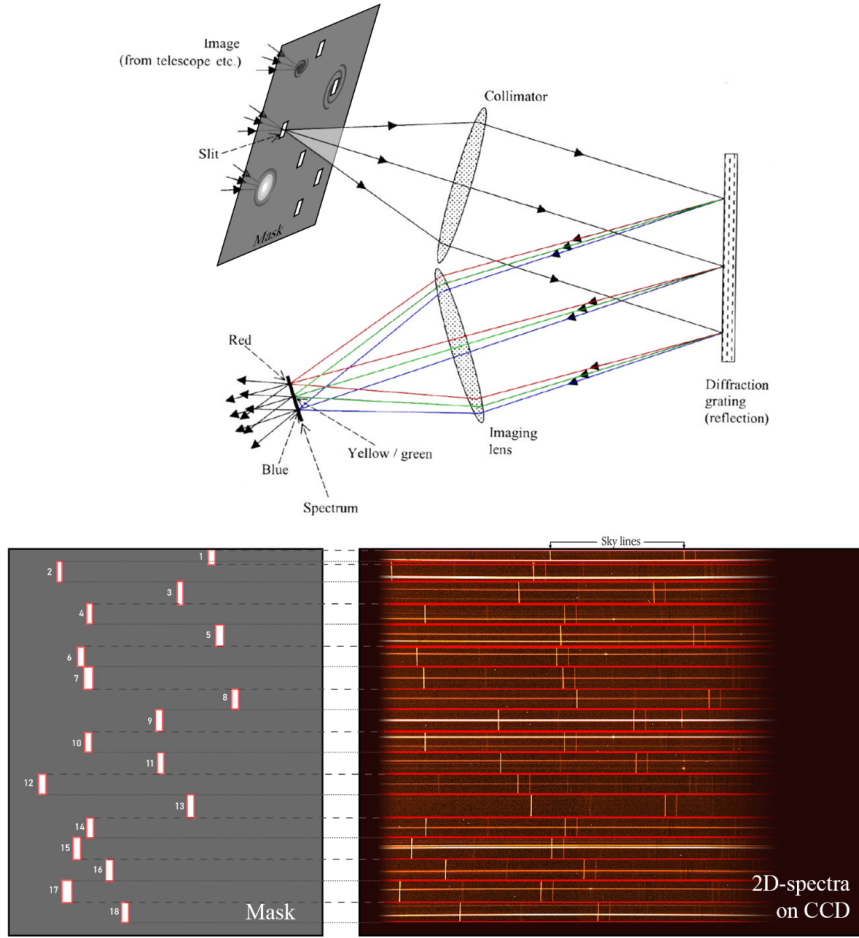


**Figure 1.2:** *Upper* — The optics of multi-object spectrograph (MOS) loading a mask with slits placed on the focal plane. *Lower Left* — A mask design example with 18 slits (in red rectangles). *Lower Right* — The two-dimensional spectra (2D spectra or spec2d's) that passed through the mask and horizontally diffracted by the grating. Each horizontal cut-off bounded by pairs of upper and lower red lines is the spectrum corresponding to a slit. In the image, some vertical lines that extend across the slit are sky emission lines illuminated by the atmospheric airglow. The horizontal continuum is the actual spectra from the targeted sources. The spec2d image is an exposure of NGC 330 taken from VLT/FORS1 (<https://www.eso.org/public/spain/images/eso9846d/>).

## 1.3 Kinematic Lensing

“Kinematic Lensing” (hereafter KL) is an approach that utilizes both imaging galaxy shape information and kinematics from slit-spectroscopy for breaking the degeneracy between intrinsic shape and weak-lensing shear. Huff et al. (2013) introduced the KL idea and provided a methodology to infer the unobservable intrinsic galaxy shape by utilizing the light-of-sight rotational velocity derived from the galaxy spectra (see Section 1.3.1) and applying the Tully-Fisher scaling relation for galaxy rotational speed (see in Section 1.3.2).

Spectroscopy is a key tool for KL analysis. Due to the Doppler shift, a spectrum provides extensive kinematic information and correlates with the velocity offset of observables relative to their rest frames. Features on the galaxy spectrum, such as absorption and emission lines, are fingerprints that reveal the dynamical properties and formation histories of galaxies. For example, the **light-of-sight velocity**, galaxy’s stellar and gas dynamics, and projected radiative geometry of astronomical objects can be constrained (see [Bolton et al. 2019](#), for an Astro2020 review). With known template spectra, more properties embedded in spectra, such as the redshift, the galaxy classification, and chemical composition, can also be revealed.

Spectrograph differs in telescope designs and the convenience of manufacturing observer-defined components (e.g., masks and slits). An observation usually targets multiple objects within the telescope’s field of view (FoV) and prefers the multi-object spectrograph (MOS), accompanied by an assembly of integral-field units (IFUs) or a mask with multiple slits as shown in Figure 1.2.

### 1.3.1 Rotation Curves

KL focuses on the spectra of lensed galaxies. Assuming a galaxy with a disk, such as a spiral galaxy, the rotational velocity ( $V$ ), inferred from the emission by stellar component and gas, grows sharply with galactic distance ( $R$ ) and becomes constant at a few of kpc. This paper assumes a circularly symmetric rotational velocity profile to fit the observed rotation curves. The velocity profile is given by an arctan function ([Courteau 1997](#), [Green et al. 2014](#)):

$$V(R) = \frac{2V_a}{\pi} \arctan\left(\frac{R}{R_t}\right), \quad (1.4)$$

where  $V$  is the rotational velocity,  $R_t$  is the transition radius between the rising and flat components of the rotation curve, and  $V_a$  is the asymptotic circular velocity of  $V(R)$  as  $R \rightarrow \infty$ .

A galaxy may have an inclination/orientation,  $\sin(i)$ , at an angle ( $i$ ) oriented from the face-on case. Hence, the map of the projected velocity field in polar coordinates,  $(r, \phi)$ , can be written as

$$\Delta v_{\text{los}}(r, \phi) := V(R) \cos(\phi) \sin(i) = \frac{2V_a}{\pi} \cos(\phi) \sin(i) \arctan\left(\frac{r(\phi)}{r_t(\phi)}\right), \quad (1.5)$$

where  $r = R \cos(\phi)$  and  $r_t = R_t \cos(\phi)$  are projected  $R$  and  $R_t$  respectively.  $\Delta v_{\text{los}}(r, \phi)$  is the offset of the light-of-sight rotational velocity relative to the galaxy’s mean velocity. Figure 1.3 gives an example of the rotation curve measurement and how slit-spectroscopy is applied. The *middle panel* is an inclined disk galaxy, and  $\sin(i)$  represents the galaxy’s orientation to be measured. If designing a slit with a  $\phi = 45^\circ$  position angle (PA), the velocity field along the slit will have a

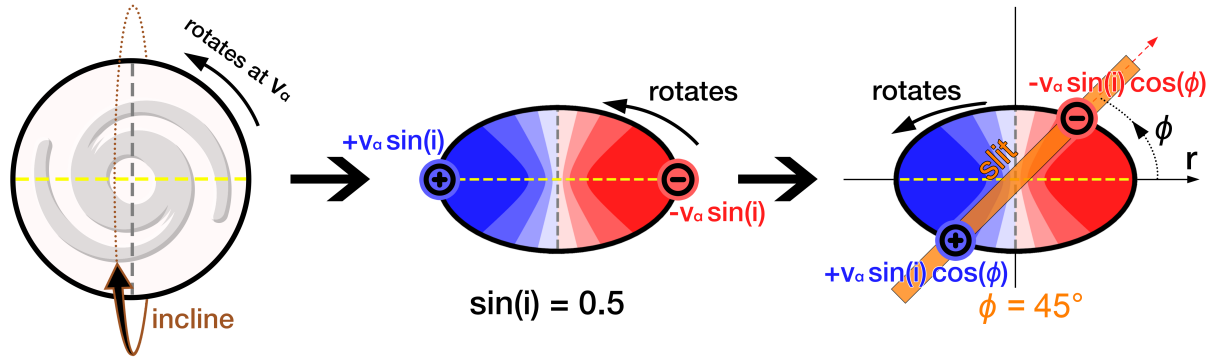


Figure 1.3: The velocity field when inclination angle  $i = 30^\circ$  and slit angle  $\phi = 45^\circ$ . In the *left panel*, the edge of the galaxy disk (in the solid black circle) rotates at a speed of  $V_a$  parallel to the page, corresponding to the  $r \gg r_t$  case in Equation 1.5. The *middle panel* describes that the galaxy disk plane is inclined, with an angle of  $i = 30^\circ$  to the celestial sphere (i.e.,  $90^\circ - i = 60^\circ$  between the galaxy disk and the observer's light of sight). The major axis of the projected disk (plotted in the yellow dashed line) then has a light-of-sight speed of  $V_a \sin(i)$ , pointing out of the paper on the left end, and in the paper on the right end. The *right panel* has a slit that is placed with an angle of  $\phi$  rotating from the major axis. The one-dimensional kinematic information can be obtained from the slit and the spectrum thereof.

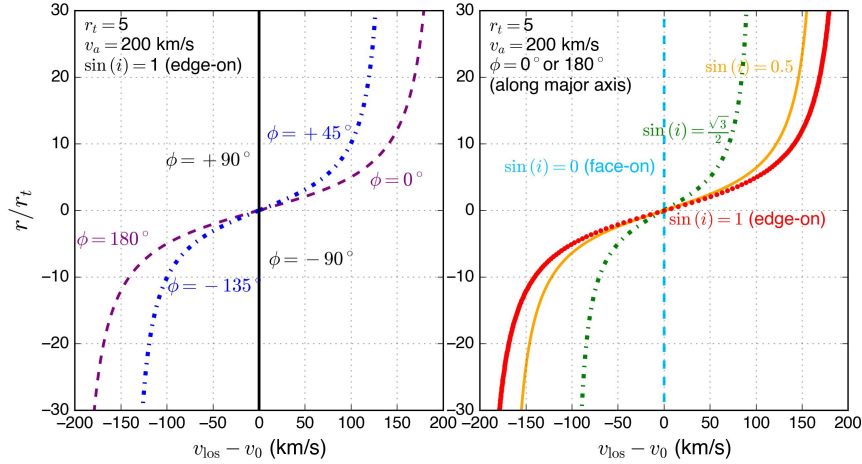


Figure 1.4: *Left* — Rotation curves in polar coordinates on the projected plane for an extreme case: the galaxy is seemed edge-on, i.e.,  $i = 90^\circ$ . *Right* — But measured along the major axis of the galaxy ( $\phi = 0$ ).

velocity of  $V_a \sin(i) \cos(\phi)$  as  $r \gg r_t$ .

Figure 1.4 demonstrates the  $\phi$  and  $i$  dependences of Equation 1.5 and corresponding rotation curves. Note that the velocity space (horizontal axis) can be converted into wavelength space in the spectrum by

$$\Delta\lambda = c \frac{\lambda - \lambda_0}{\lambda_0}, \quad (1.6)$$

where  $\lambda_0$  is the systematic wavelength of the emission line and  $c$  is the speed of light. Hence,

rotation curves are easily identified in the galaxy's spectra. For one galaxy, various rotation curves can be observed for different slit PA ( $\phi$ ) cases (Figure 1.4 *left panel*). Once the slit PA is known (*right panel*), for example of  $\phi = 0$ , the rotation curve will be fitted with the above models, **yielding the light-of-sight rotational velocity**  $v_{\text{spec}} := V_a \sin(i)$ , with  $V_a$  to be solved shortly.

### 1.3.2 Tully-Fisher Rotational Speed

Spiral galaxies exhibit disk rotation patterns; a circular rotational speed,  $v_{\text{rot,TF}}$ , can be estimated from the Tully-Fisher scaling relation (Tully & Fisher 1977), which depends on the galaxy's luminosity, usually in terms of absolute magnitude in the  $r$ -band,  $M_r$ :

$$\log(v_{\text{rot,TF}}) = a(M_r - M_0) + b, \quad (1.7)$$

where  $M_0$  is a pivot value,  $b$  is the intercept, and  $a$  is the slope with typical values of  $a \sim -0.1 \log(\text{km s}^{-1})/\text{mag}$  (e.g., Reyes et al. 2011). These values may vary depending on the selected photometric filters and the ages of galaxy populations. The asymptotic velocity  $V_a$  is then replaced by the Tully-Fisher rotational speed,  $v_{\text{rot,TF}}$ , i.e.,

$$V_a = v_{\text{rot,TF}}. \quad (1.8)$$

This builds up a key relation in KL to determine **the galaxy orientation**:

$$\sin(i) = \frac{v_{\text{spec}}}{v_{\text{rot,TF}}} = \frac{\lim_{r \rightarrow \infty} [\Delta v_{\text{los}}(r, 0)]}{v_{\text{rot,TF}}}. \quad (1.9)$$

### 1.3.3 Expectations of Kinematic Lensing

Kinematic lensing uses the emission-line features from spectra and improves three key systematic uncertainties in traditional weak lensing measurements:

- 1. Reduced Shape Noise.** This is the key to measuring the intrinsic shape with the source galaxy's inclination and velocity/frequency field. Besides the slit spectroscopy strategy in Section 1.3.2 and 1.3.1, velocity/frequency fields can be directly obtained by using those spectrographs with IFUs.
- 2. Redshift Uncertainties.** This is not surprising that spectroscopic redshifts have better precision given the uncertainties of the photometric redshifts (e.g.,  $\sigma[\Delta z_{\text{phot}}/(1+z_{\text{phot}})] \sim 0.05$  by Tanaka et al. 2018). Kinematic lensing utilizes a spectrograph with a common resolving

power of  $R = 1500$  yields a redshift measurement uncertainty of  $\sigma[z_{\text{spec}}] = (1 + z_{\text{spec}})/R = 0.001$  for a source galaxy at  $z_{\text{spec}} = 0.5$ , which is  $\sim 50$  times better than photometric redshift uncertainty.

3. **More Bright Galaxy Samples.** Traditional lensing measurement must include low signal-to-noise galaxies (e.g.,  $J + H$  band combined SNR>18 by [Eifler et al. 2021](#)) to increase the sample size and statistical precision. However, kinematic lensing focuses on bright ( $r$ -band SNR>50), emission-line-well-resolved, unblended (relatively isolated) galaxies, improving the photometric shape measurement for smaller biases ([Pranjal et al. 2023](#), [Xu et al. 2023](#)).

Compared to the shape noise from the weak lensing measurement of  $\sigma_\epsilon \sim 0.26$  in Section 1.2, kinematic lensing makes it as low as  $\sigma_\epsilon^{\text{KL}} = 0.04$  based on recent mock observations (see details in [Xu et al. 2023](#)). Therefore, the KL shape noise is dominated by the Tully-Fisher relation intrinsic scatter. KL assumes  $v_{\text{rot,TF}} = v_a$  (see Section 1.3.2). At a  $R = 2000$  spectral resolving power and a spectral SNR=30, [Pranjal et al. \(2023\)](#) report that  $\sigma_\epsilon^{\text{KL}}$  is insensitive to the Tully-Fisher relation intrinsic scatter, yielding an average of  $\sigma_\epsilon^{\text{KL}} = 0.06$ .

Other studies on weak lensing shape noises also highlighted the importance of the velocity fields inferred by spectroscopy. [Gurri et al. \(2020\)](#) used the lens-source position relation to infer  $v_a$ , rather than KL using the Tully-Fisher relation, which they called “precision weak lensing” measurements for galaxy-galaxy lensing systems. [Gurri et al. \(2021\)](#) and [DiGiorgio et al. \(2021\)](#) developed the precision weak lensing measurement with a relatively small effective shape noise  $\sigma_\epsilon = 0.017\text{--}0.031$ . [Wittman & Self \(2021\)](#) presented the first comprehensive KL shape noise study with the Tully-Fisher relation involved, giving a shape noise of  $\sigma_\epsilon^{\text{KL}} \sim 0.04$ .

# Chapter 2

## Kinematic Lensing on “Weighing the Giants” Galaxy Clusters

The previous chapter introduced kinematic lensing (KL), which has been assessed through theoretical justifications and simulated mock observations for joint analysis of galaxy imaging and slit spectroscopy. However, real observation data has not been examined for KL yet. This chapter will mine archived slit-spectroscopic data and dig into KL’s potential in reducing shape noise.

### 2.1 Target Selection

We selected the sample of galaxy clusters studied in the *Weighing the Giants* project by [von der Linden et al. \(2014a\)](#), [Kelly et al. \(2014\)](#), and [Applegate et al. \(2014\)](#). The *Weighing the Giants* (hereafter WtG) clusters have robust weak-lensing shape measurement at hand, calibrated masses from X-ray observations ([von der Linden et al. 2014b](#)), spanning an intermediate redshift range of  $0.15 < z_{\text{cl}} < 0.7$ . The WtG cluster sample has 51 clusters, with archives of (1) photometric imaging observed with Subaru/SuprimeCam and CFHT/MegaPrime, (2) maps of the total mass distribution measured from weak lensing, (3) extended *Chandra* X-ray emission from each cluster, (4) central galaxy determination, and (5) photometric redshifts.

We used the spectroscopic archived data from Keck/DEIMOS ([Faber et al. 2003](#)), a multi-object spectrograph (MOS) with slit and mask design. The target clusters were selected from the WtG sample with available spectra from Keck/DEIMOS data releases, including some clusters that were the MACS targets in the sample of [Mantz et al. \(2010a,b\)](#). In summary, the select clusters should: (I) be from the WtG sample, and (II) have available MOS spectra from Keck/DEIMOS.

This gave 10 clusters that satisfy the above criteria and we added 10 more clusters in our

Table 2.1: Clusters Observed from Keck/DEIMOS and Rotation Curves

	Cluster (1)	RA (deg) (2)	Dec. (deg) (3)	$z_{\text{Cl}}$ (4)	Mask (5)	Grating (6)	Date (7)	Set (8)	$N_{\text{slits}}$ (9)	$N_z$ (10)	$N_b$ (11)	$N_c$ (12)	$N_{bc}$ (13)
1	A2552	347.88818	3.63514	0.302	25521B	1200G	2015-12-13	A	143	72	9	7	2
2	A611	120.23674	36.05709	0.288	sna611	600ZD	2012-10-15	E	48	16	3	2	1
3	A1758N	203.18111	50.54398	0.279	ejc	600ZD	2018-07-16	I	76	22	0	0	0
4	A1758N	203.18111	50.54398	0.279	ejc1	600ZD	2018-07-17	C	63	22	1	0	0
5	A1758N	203.18111	50.54398	0.279	ejc2	600ZD	2018-07-18	D	39	17	2	4	0
6	M1115	168.96617	1.49861	0.355	sn1115	600ZD	2012-02-26	B	120	60	37	15	11
7	M1115	168.96617	1.49861	0.355	1115m1	600ZD	2014-02-25	A	147	76	15	20	3
8	M1115	168.96617	1.49861	0.355	jc9	600ZD	2015-06-16	B	31	11	0	4	0
9	A2261	260.61244	32.13275	0.224	a2261aB	1200G	2014-07-01	A	63	41	37	28	24
10	A2261	260.61244	32.13275	0.224	a2261b	1200G	2014-07-01	B	66	31	31	25	25
11	A2261	260.61244	32.13275	0.224	a2261c	1200G	2014-07-01	C	62	27	26	22	21
12	A2261	260.61244	32.13275	0.224	a2261d	1200G	2015-06-18	A	65	25	25	13	13
13	A2261	260.61244	32.13275	0.224	a2261c	1200G	2015-06-18	B	62	30	29	22	20
14	A2261	260.61244	32.13275	0.224	a2261b	1200G	2015-06-18	C	64	30	28	20	17
15	A2261	260.61244	32.13275	0.224	a2261a	1200G	2015-06-18	D	65	32	29	26	23
16	A370	39.97186	-1.57718	0.375	A37017B1	1200G	2017-09-28	A	121	14	1	4	1
17	A370	39.97186	-1.57718	0.375	A37017B2	1200G	2017-09-28	B	103	11	4	7	1
								Total	1338	451	277	219	162
								Non-duplicate and Non-Stellar Objects Total	1125	443	187	149	105

COLUMN DEFINITIONS — (1) Cluster name; \*\*“M1115” is short for “MACS J1115.8+0129”; (2–3) The cluster’s RA and Dec at the epoch of J2000.0 and in the unit of degrees; (4) Cluster redshift  $z_{\text{Cl}}$ ; (5) Mask name defined by the observer; (6) The grating name with numbers in the unit of lines/mm; (7) Observation date; (8) Grating’s configuration containing science images; (9) Number of slits  $N_{\text{slits}}$ ; (10) Number of secure redshifts  $N_z$ ; (11) Number of background secure redshifts  $N_b$  that are 0.1 greater than cluster redshift (i.e.  $z > z_{\text{Cl}} + 0.1$ ); (12) Number of rotation curves discovered  $N_c$ ; (13) Number of background rotation curves  $N_{bc}$ .

dataset. In particular, the cluster Abell 2261 (hereafter A2261) was studied for kinematic lensing and observed (Program ID: N177D, PI: T. Eifler 2015) by using 7 masks, making its importance in this study. The size of this cluster sample is 20 and the number of masks is 57. Since the current research stage focuses on the slit-spectroscopy observation test for KL, we selected a subset (6 out of 20) as the preliminary Keck/DEIMOS cluster sample. Table 2.1 lists the observation details. In summary, we have a sample size of 6 selected clusters with 17 masks that span a redshift range of  $z_{\text{Cl}} = 0.224\text{--}0.375$ .

Table 2.2: Keck/DEIMOS Characteristics

Spectroscopic Grating (lines/mm)	Blaze Wavelength (Å)	Dispersion Scale (Å/pixel)	FWHM Spectral Resolution (1'' slit) $\Delta\lambda$ (Å)	Resolving Power $R$
600	7500	0.65	4.7	1606
1200	7500	0.33	1.5–2.1	3571–5000

SOURCE — <https://www2.keck.hawaii.edu/inst/deimos/specs.html>

## 2.2 Data Reduction

Section 1.3 introduced the importance of slit spectroscopy for kinematic lensing measurements and highlighted how emission line features contribute to solving galaxy orientations and reducing the shape noise. The key here is to find a spectrograph that captures common emission lines (to be discussed below), and more fortunately, resolves some of the strong emission lines, such as [O II] $\lambda\lambda 3727,3729$  doublet.

### 2.2.1 Keck/DEIMOS

DEIMOS<sup>1</sup> (DEep Imaging Multi-Object Spectrograph; Faber et al. 2003) is a visible-wavelength, faint-object, multi-slit imaging spectrograph operating at the Nasmyth focus of the Keck II telescope. The 600–1200 lines/mm gratings result in a  $\leq 0.65$  Å/pixel dispersion and a spectral resolution around 1.5–4.7 Å (Table 2.2).

Since the redshifts of clusters are around  $z = 0.3$  and Keck/DEIMOS has a wavelength range of 4100–11000 Å, I search for the primary spectral line features of Ca H&K $\lambda\lambda 3933,3968$  doublet absorption lines and [O II] $\lambda\lambda 3727,3729$  doublet emission lines. Note that the 600 lines/mm grating cannot resolve [O II] due to its spectral resolution of  $\Delta\lambda = 4.7$  Å being greater than the 2 Å separation of the doublet, hence the [O II] appear as a single emission line. Other features are also remarkable, such as H  $\gamma$   $\lambda 4340$ , H  $\beta$   $\lambda 4861$ , [O III] $\lambda\lambda 4959,5007$  doublet, N II  $\lambda\lambda 6548,6584$  doublet, H  $\alpha$   $\lambda 6563$ , and [S II] $\lambda\lambda 6716,6731$  doublet.

### 2.2.2 Raw and Calibration Data

The raw data with corresponding calibration files for our cluster sample is retrieved from the Keck Observatory Archive Data Access<sup>2</sup> with parameters: Instrument = DEIMOS, Location = cluster's RA/Dec coordinates with a search radius of 300 arcsec, and Dispersion = mos. The data

---

<sup>1</sup><https://www2.keck.hawaii.edu/inst/deimos/>

<sup>2</sup><https://koa.ipac.caltech.edu/cgi-bin/KOA/nph-KOALogin>

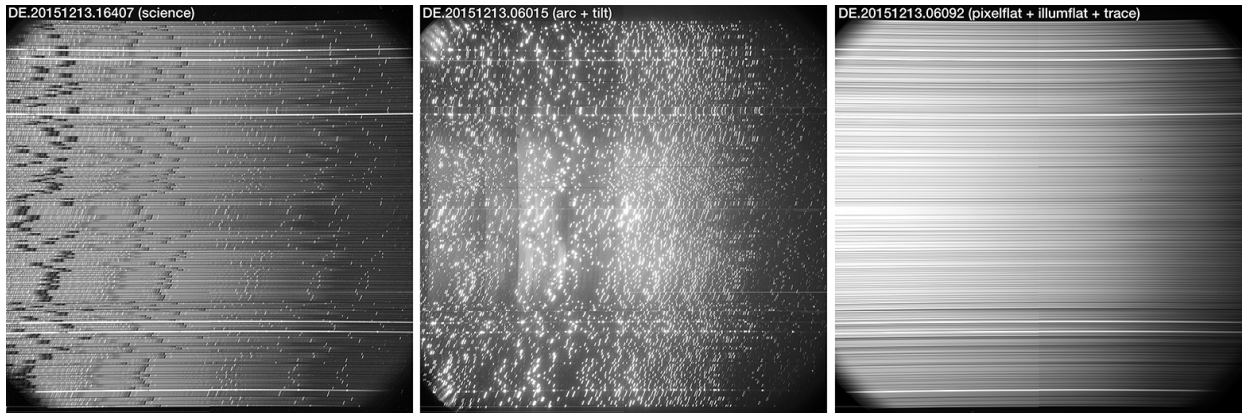


Figure 2.1: Raw and calibration CCD  $8192 \times 8192$  pixel<sup>2</sup> images of A2552. *Left panel* — Science image of the cluster A2552’s spectra. It captures the lights from actual objects dispersed by the Keck/DEIMOS spectrograph and the 1200G grating. Each horizontal strip corresponds to an object and a slit thereof, which is called a 2D spectrum. *Middle panel* — Short vertical(-ish) bright “arc lines” in each slit’s 2D spectrum. *Right panel* — “Flat image” to calibrate with the illumination sensitivity on CCD.

was downloaded as multiple exposures of science images in FITS format. For each dataset, we also retrieve the following calibration data: arc, tilt, trace, and flat images as shown in Figure 2.1.

### 2.2.3 PypeIt: A Reduction Pipeline

PYPEIT<sup>3</sup> (Prochaska et al. 2020) is a Python package for the semi-automated reduction of spectroscopic data for popular MOS instruments. PYPEIT performs normal calibration corrections<sup>4</sup>, such as flat-fielding by using the flat image for slit edge tracing and relative pixel efficiency correction, and dark frame/bias subtractions by overscan-subtracting the raw image and optionally correcting for bias and dark current.

Since the CCD image does not contain wavelength information, it is vital to take images under a lamp source with the same spectrograph setup as when the science image is taken. We explain how PYPEIT runs the wavelength calibration, summarizes the slit information, and co-adds the multiple reduced and calibrated images as follows.

#### Slit Identification

PYPEIT reads the trace image and FITS header information to identify which slit corresponds to which strip on the CCD science 2D spectrum, yielding a list of slits with corresponding targets’ information, such as RA/Dec and slit PA.

<sup>3</sup>PYPEIT documentation: <https://pypeit.readthedocs.io/en/release/>

<sup>4</sup>[https://pypeit.readthedocs.io/en/release/calibrations/image\\_proc.html](https://pypeit.readthedocs.io/en/release/calibrations/image_proc.html)

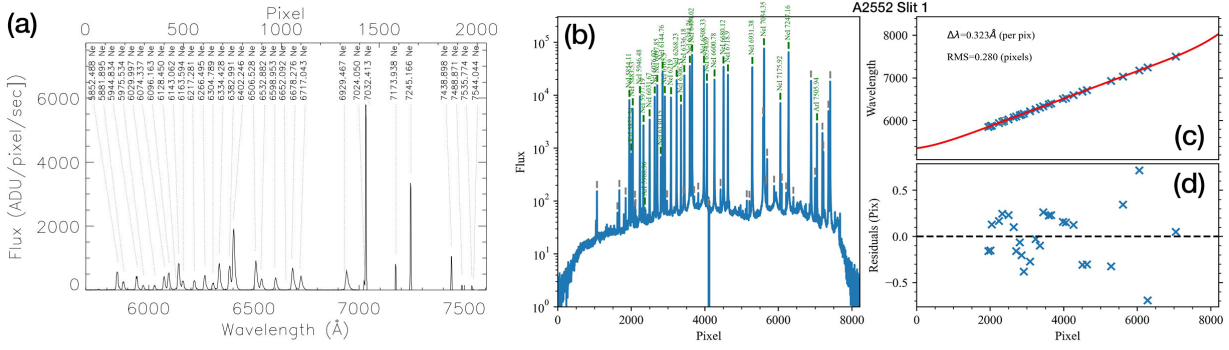


Figure 2.2: Panel (a) – Vacuum Neon-lamp spectrum ([https://www2.keck.hawaii.edu/inst/lris/arc\\_calibrations.html](https://www2.keck.hawaii.edu/inst/lris/arc_calibrations.html)). Panels (b-d) — Wavelength calibration for the Slit 1 (RA=347.81934°, Dec=3.58599°) of cluster A2552. Panel (b) identifies the arc lines (in green) and maps a relationship between pixels and wavelengths. Panel (c) applies a second-polynomial fit (in red) with residual values to check in Panel (d).

## Wavelength Calibration

This procedure uses an arc lamp filled with one element, such as  $^{10}\text{Ne}$  (neon), or a mixture of multiple noble elements. With known<sup>5</sup> wavelengths of the arc-lamp lights at rest frame (Figure 2.2a), PYPEIT automatically identifies arc lines in the spectrum and determines the mapping relationship between spatial pixels and wavelengths (Figure 2.2b). PYPEIT gives an analytic polynomial fit to the pixel-wavelength mapping as shown in Figure 2.2c. Figure 2.2d shows the residual values, where the ideal residual is below 1 pixel on the root-mean-squared (RMS) average. A typical polynomial fit has second or third order, depending on which RMS thereof is obtained minimally. Those with automatically generated bad fits ( $\text{RMS} \geq 1$  pixel) are manually corrected, and the wavelength calibration is re-performed.

Some arc lines in Figure 2.1 *middle panel* are tilted and not perpendicular to the horizontal strip. This is due to distortion within the spectrograph and the tilted slits, with the slit position angles (PA) that may align with their target galaxy’s major axis (make  $\phi = 0$  in Equation 1.5) to capture the velocity curves. The slit’s PA will be an important outcome parameter in this study.

## Object Finding and Sky Line Subtraction

There may be sky lines not from the target object but across the faint spectrum continuum. Sky lines are a series of lines illuminated by atmospheric airflow. PYPEIT first finds the assembly of the most probable sources (e.g.,  $\text{SNR} > 5\sigma$  where  $\sigma$  is the standard deviation of the slit’s overall SNR) and treats it as the 2D object model of the slit. Then, the sky subtraction algorithm finds and

<sup>5</sup>[https://www2.keck.hawaii.edu/inst/lris/arc\\_calibrations.html](https://www2.keck.hawaii.edu/inst/lris/arc_calibrations.html)

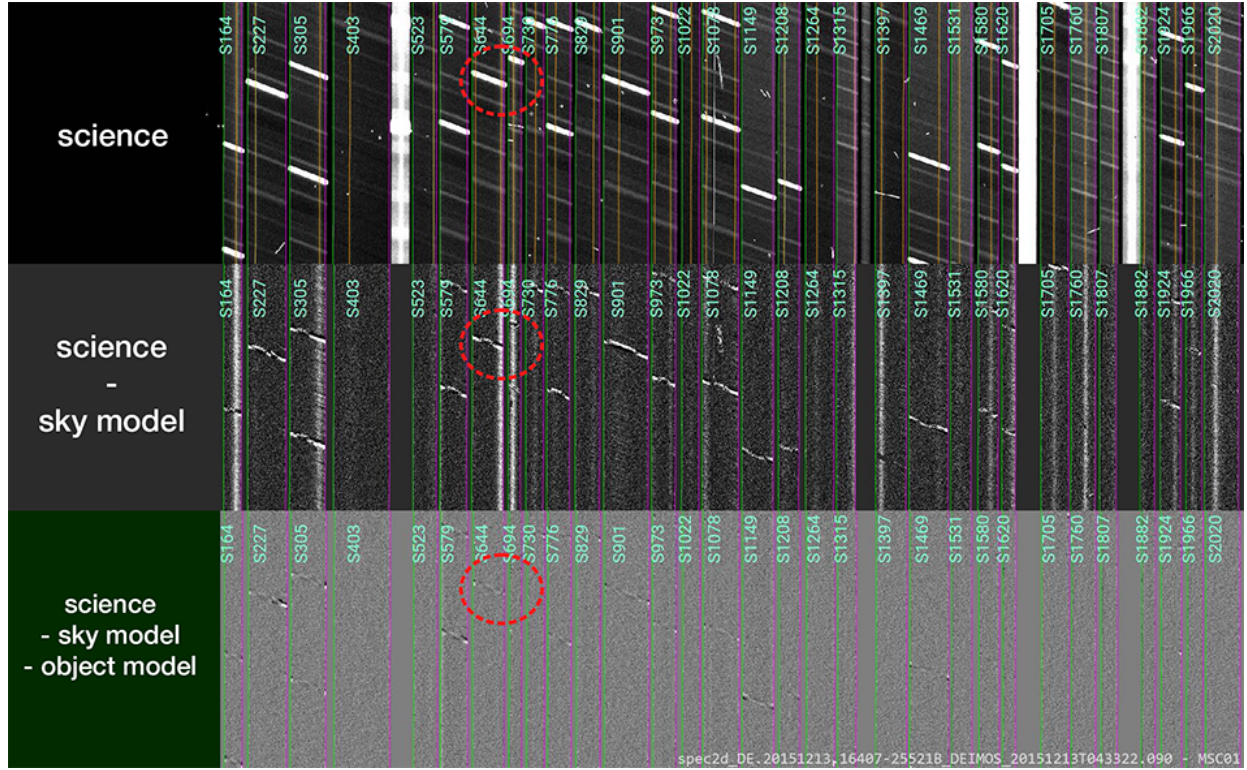


Figure 2.3: Sky line subtraction by four steps. All panels of steps are the same portion of the CCD image, where the red dash circles explicitly indicate the same CCD location for better visualization and comparison.

defines the parallel pixels that are next to the object as the sky model, as shown in Figure 2.3.

The 1D spectrum models are extracted from 2D objects and stored in arrays of flux and wavelength. The extraction creates a mask for 2D objects with a window size defined by either the trace or the full-width-of-half-maximum (FWHM) of the 2D-fitted spatial profile. The flux of extracted 2D object is integrated into a 1D spectrum model.

## Co-addition

Charged particles may hit the CCD and leave anomalous tiny lines on the image, called cosmic rays. To eliminate the cosmic rays, we let PYPEIT co-add each exposure of all science images that were reduced after all the previous steps above. We set the methods of co-adding multiple frames to the weighted mean, which computes an average image using uniform weighting. This gives a co-added 2D spectra image, and the 1D spectrum extraction (see previous paragraph) is then re-performed on the 2D image.

In summary, PYPEIT finishes the reduction for each observation (per mask) and outputs a co-added CCD image containing all 2D spectra, an extracted co-added 1D spectrum data cube in FITS

format, and a slit table in TXT format containing slit RA/Dec, slit PA, the extracted object’s pixel positions on the image, and median signal-to-noise ratio (SNR).

## 2.3 Results

### 2.3.1 Spectroscopic Redshifts

#### Spectrum Cutting-off by Slit

We develop `pypeittospecpro`<sup>6</sup> (a Python script) and the co-added slit TXT table, to split co-added all-object spectra into each combination of 1D spectrum and 2D spectrum per object/slits. There are 1338 spectra for all slits in our cluster sample and the amount for each cluster is listed in Table 2.1. Since different slits may share the same target, these 1338 spectra are for 1125 targets of slits after removing duplicated slits.

#### Templates, Tools, and Measurements

Spectral templates are required for the fittings in the redshift measurements. We utilize the spectral templates from SDSS, PEGASE ([Fioc & Rocca-Volmerange 1997](#)) stellar population synthesized model. Multiple stellar spectra ranging from A0 to M6 types are additionally added in the case of the slit’s stellar target. The templates are listed in Table 2.3.

We develop FIREFLY<sup>7</sup> (Fast Initial REdshift Fitting of cLuster galaxY) Python package, to guess the approximate redshift solutions with a probability distribution. FIREFLY is designed to use two or more user-selected spectral templates for rapid fittings. The FIREFLY quickly forecasts the redshift fitting analyses and it benefits from the philosophy of avoiding the processing time of manual redshift measurement, which needs multiple attempts on template selection, automatic redshift inspection, and best spectroscopic redshift decision.

We use SPECPRO ([Masters & Capak 2011](#)), an IDL-based software, to present multiple feasible redshift solutions from fitting a number of spectral templates with emission and absorption features. In SPECPRO GUI, the template spectrum overlays with the observed spectrum along with the emission and absorption lines marked at the best-fitting scale. SPECPRO shows its convenience of handling manual redshift adjustments, where we can move the template with lines bluewards (for smaller redshift adjustments) or redwards (for larger redshift adjustments) to fit with the template best visually. We inspect all redshifts from this study by SPECPRO.

---

<sup>6</sup><https://github.com/ABeck12/Kinematic-Weak-Lensing-Group/blob/main/Specpro/pypeittospecpro.py>

<sup>7</sup><https://github.com/jiyundi/firefly>

Table 2.3: Spectral Templates For Cross-Correlation

Template	Source	Dispersion Scale (Å/pixel)	Spectral Resolution $\Delta\lambda$ (Å)	Resolving Power $R$
LBG Shapley	Lyman break galaxy <sup>o</sup>	1.0	8–12	417–625
SDSS QSO	Broad-line quasar <sup>△</sup>	1.0	2	2000
SDSS LoBAL	Low-ionization BAL quasar <sup>†</sup>	0.7	1.8–5.1	2000
SDSS HiBAL	High-ionization BAL quasar <sup>†</sup>	0.7	1.8–5.1	2000
SDSS Luminous Red	Luminous red galaxy*	1.6	1.8–5.1	2000
SDSS Early Type	Early-type galaxy*	2.1	1.8–5.1	2000
SDSS Low Emission	Low-emission-peak galaxy*	2.1	1.8–5.1	2000
SDSS Normal Emission	Normal-emission-peak galaxy*	2.1	1.8–5.1	2000
SDSS High Emission	High-emission-peak galaxy*	2.1	1.8–5.1	2000
SDSS Late Type	Late-type galaxy*	2.1	1.8–5.1	2000
Red galaxy	PEGASE passive galaxy	2.0	1.4	
Green galaxy	PEGASE early spiral	2.0	1.4	
Blue galaxy	PEGASE spiral/starburst	2.0	1.4	
A0 star	A0 stellar templates‡	5	5	500
F0 star	F0 stellar templates‡	5	5	500
G0 star	G0 stellar templates‡	5	5	500
K0 star	K0 stellar templates‡	5	5	500
M0 star	M0 stellar templates‡	5	5	500
M6 star	M6 stellar templates‡	5	5	500

NOTE — Sources: <sup>o</sup> [Shapley et al. \(2003\)](#), <sup>△</sup> [Schneider et al. \(2010\)](#), <sup>†</sup> [Reichard et al. \(2003\)](#),

‡ [Pickles \(1998\)](#), and \*SDSS DR2 ([Abazajian et al. 2004](#)) spectral templates:

<https://classic.sdss.org/dr5/algorithms/spectemplates/index.php>

## Redshift Reliability

We assigned the “confidence” flags to indicate the reliability of the redshift measurement from SPECPRO:

- 3 = Secure (two or more lines are identified and outcome one redshift);
- 2 = Likely (one line is identified and outcomes a redshift);
- 1 = No determination.

Confidence flags mainly depend on the object SNR and telluric lines (overlying with atmosphere absorption bands).

A spectrum may show the [O II] emission line only. When the used grating results in a good spectral resolution of  $\Delta\lambda < 2\text{\AA}$ , the [O II] emission appears as a doublet, and now, confidence=3. However, [O II] doublet may be blended into one single line as demonstrated in Figure 2.4 *lower panel*. Hence the redshift confidence must be set to 2.

For a target observed in multiple observations, we cross-check the spectra and compare redshifts between masks used in observations, thus the final redshift is determined with a flag = 3.

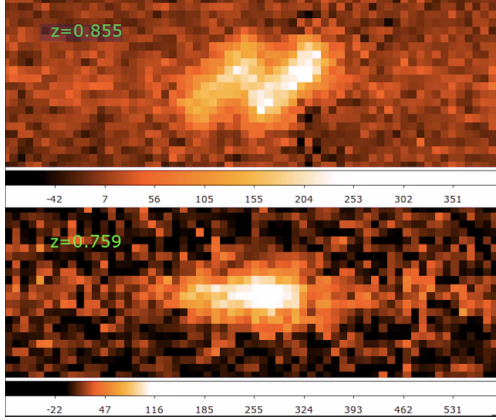


**Figure 2.4:** *Upper panel* — Well-resolved  $[\text{O II}]\lambda\lambda 3727, 3729$  doublet in spectra of one galaxy ( $\text{RA}=216.38017^\circ$ ,  $\text{Dec}=-0.86529^\circ$ ). *Lower panel* — Blended  $[\text{O II}]$  in the spectrum of another galaxy ( $\text{RA}=216.39340^\circ$ ,  $\text{Dec}=-0.77723^\circ$ ). Both spectra of the galaxies are taken under the same  $\Delta\lambda = 2\text{\AA}$  spectral resolution, referred from [Di et al. \(2023\)](#)

**Table 2.4: Redshift Table of A2552**

Slit	Redshift	RA	Dec.	Slit PA	SNR	Lines	Confidence	Rotation Curve
1	0.2036	347.81923	3.58582	32.3	9	MgI,NaI	3	-
2	-	347.82996	3.57436	32.3	0	-	1	-
3	-	347.82763	3.58197	32.3	5	-	1	-
4	-	347.84384	3.56478	32.3	0	-	1	-
5	-	347.84466	3.57034	32.3	1	-	1	-
6	-	347.83836	3.58228	32.3	2	-	1	-
7	-	347.83836	3.58228	32.3	0	-	1	-
8	0.3038	347.84285	3.57961	32.3	9	Gband,MgI	3	-
⋮	⋮	⋮	⋮	⋮	⋮	⋮	⋮	⋮
13	0.1831	347.85007	3.58390	32.3	1	$[\text{O III}], \text{H}\beta$	3	Tilted
⋮	⋮	⋮	⋮	⋮	⋮	⋮	⋮	⋮
67	0.2515	347.90510	3.66308	32.3	4	$\text{H}\beta, [\text{O III}]$	3	Tilted
⋮	⋮	⋮	⋮	⋮	⋮	⋮	⋮	⋮
77	0.3993	347.94812	3.64090	32.3	1	$\text{H}\gamma, [\text{O III}]$	3	Tilted
⋮	⋮	⋮	⋮	⋮	⋮	⋮	⋮	⋮
86	0.1200	347.94327	3.67101	32.3	14	$\text{H}\beta, \text{NII}, \text{H}\alpha, [\text{S II}]$	3	Tilted
⋮	⋮	⋮	⋮	⋮	⋮	⋮	⋮	⋮
121	0.3650	348.00765	3.70767	32.3	5	$\text{H}\beta, [\text{O III}]$	3	Y
⋮	⋮	⋮	⋮	⋮	⋮	⋮	⋮	⋮
124	0.6283	348.00862	3.71565	32.3	1	$[\text{O II}], \text{H}\gamma$	3	Tilted
⋮	⋮	⋮	⋮	⋮	⋮	⋮	⋮	⋮
141	0.3008	348.02758	3.74038	32.3	11	Gband,MgI	3	-
142	-	348.05552	3.70238	32.3	7	-	1	-
143	-	348.05206	3.70963	32.3	1	-	1	-

NOTE — “Y”/“Tilted” = rotation curves found. This table is entirely available in machine-readable format.

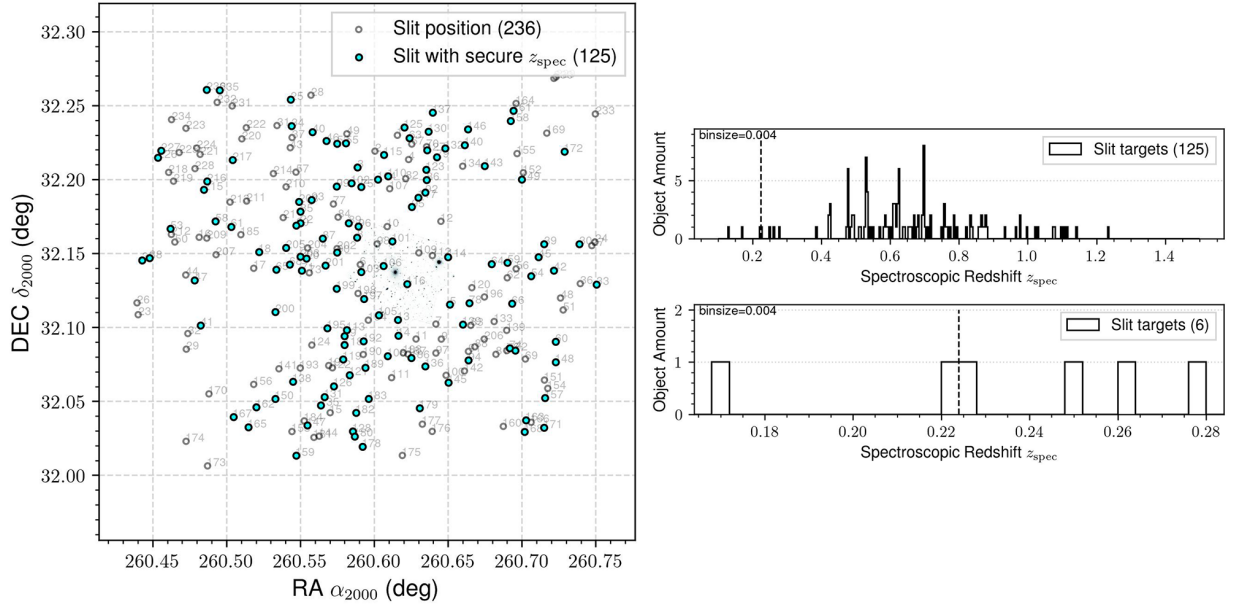


Figure 2.5: Distribution of (*left*) slit positions and (*right*) non-duplicated secure redshifts of A2261. The *top-right* is the redshift distribution for all slits and the *bottom-right* panel is a zoom-in around the cluster's redshift  $z_{\text{Cl}} = 0.224$  (marked in vertical dash lines).

All the measured spectroscopic redshifts are obtained in tables; Table 2.4 gives a portion of an example redshift table for the A2552. For the entire cluster sample, 1125 slit targets produce 451 redshifts and the confidence-flag distribution of 60, 1, and 39% for confidence = 1, 2, and 3, respectively.

### Secure Redshifts

We define a redshift as secure when confidence  $\geq 2$ . Despite 8 redshifts with confidence = 3 from the stellar spectra, there are 443 secure redshifts for non-stellar objects measured in this study. Figure 2.5 displays an example of the slit map and secure redshift distribution for all the targets of A2261 and all masks.

### 2.3.2 Rotation Curves and Velocity Fields

Figure 2.6 shows the spectra containing bright, tilted, and curved emission lines identified in M1115 (Row 6 of Table 2.1) as plotted in the *left panel* with slit numbers on their right edges, as well as the Slit 38's 1D spectrum at spectroscopic redshift  $z_{\text{spec}} = 0.7419$  (*top-right*), zoom-ins for 4 emission lines (*middle-right panels*), and 2D spectrum cut-offs at the positions of 4 emis-

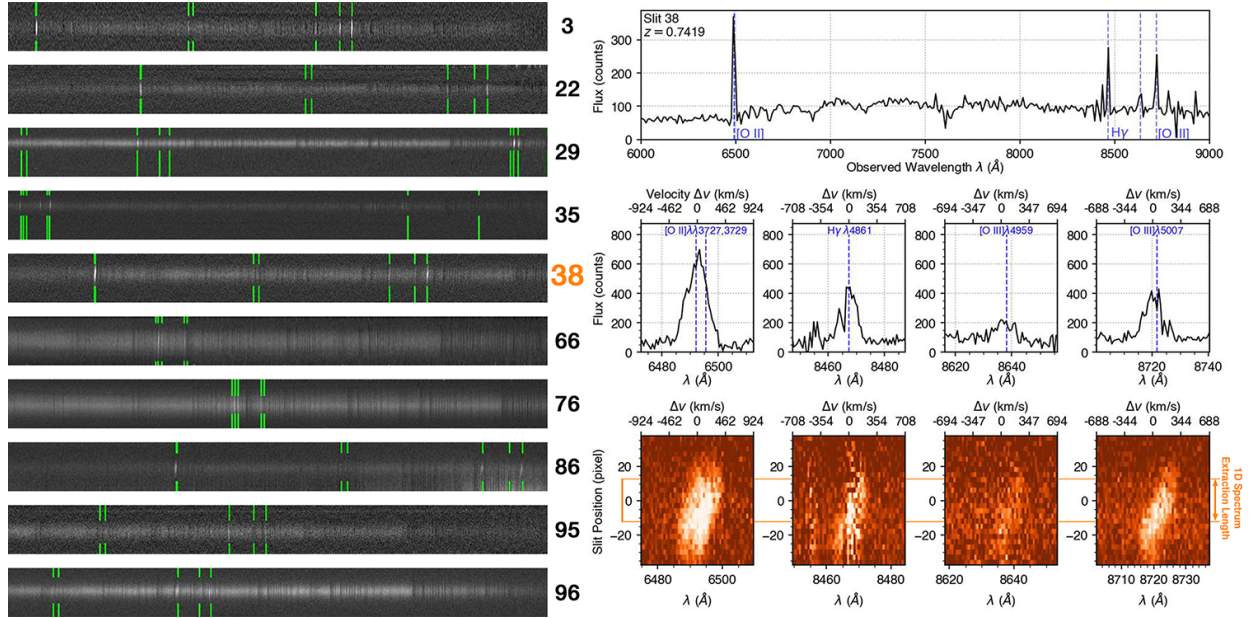


Figure 2.6: *Left* — 2D spectra of slits in M1115 (Row 6 of Table 2.1) with possible emission and absorption lines and rotation curves (highlighted in green); *Right* — Broad and zoomed 1D spectra Slit 38 ( $z_{\text{spec}} = 0.7419$ , RA=169.00939°, Dec=1.42496°), and 2D spectra with rotation curves. The 1D spectra are extracted from 2D with a PYPEIT-optimized length of 25 pixels = 1'' = 7.3 kpc (physical), where the vertical side length of each 2D spectrum is 75 pixels = 3'' = 21.9 kpc (physical), assuming  $H_0 = 70 \text{ km/s/Mpc}$ ,  $\Omega_m = 0.3$ , and  $\Omega_\Lambda = 0.3$ . Each 2D spectrum is 40 Å clipped yielding a velocity interval of  $v_0 \pm (688-924) \text{ km/s}$  (by Equation 1.6).

sion lines (*bottom-right panels*), which are exactly the rotation curves. The curved, “S”-shaped emission line behaves as two peaks in the 1D spectrum which can be observed in cases of  $\text{H}\gamma$  and  $[\text{O III}]$  panels. Unfortunately, the galactic rotation combined with  $[\text{O II}]$  doublet is poorly resolved and makes  $\lambda 3727$  blended with  $\lambda 3729$ , yielding a single, wide peak in the 1D spectrum. Instead, the width of blended lines becomes another key factor for  $[\text{O II}]$  doublet identification.

The rotation curves are turned into the KL measurement pipeline developed by Pranjal et al. (2023, in Section 4.2). We assume an idealized cluster lensing geometry with all shears perfectly tangentially-aligned. The fast-forward model (Pranjal et al. in-prep.) gives fittings of 20 free parameters<sup>8</sup>, including  $\gamma_t$ , the perpendicular shear component relative to the cluster center, which accomplishes the main goal of this thesis. Figure 2.7 compares the observed rotation curves with the best-fit model. The model fit reproduces an inclined velocity field. The best-fit model also recovers an emission map of the target galaxy and compares it with the imaging observation.

<sup>8</sup>To better display Figure 2.6, the posterior (*lower panel*) captions are moved here — From left, the 20 parameters rows are: (1) tangential shear  $\gamma_t$ , (2) maximum circular velocity constrained by Tully-Fisher rotational speed  $v_{\text{circ}}$ , (3) inclination  $\cos(i)$ , (4) intrinsic galaxy position angle  $\theta_{\text{int}}$ , (5) velocity-scale radius  $r_{\text{vscale}}$ , (6–7) disk/bulge half-light radius  $r_{\text{hl}}^{\text{disk}}/r_{\text{hl}}^{\text{bulge}}$ , (8–9) fractional disk x/y-offset  $\delta_x^{\text{disk}}/\delta_y^{\text{disk}}$ , (10–11) fractional bulge x/y-offset  $\delta_x^{\text{bulge}}/\delta_y^{\text{bulge}}$ , (12–13) image/bulge flux normalization  $F_{\text{disk}}/F_{\text{bulge}}$ , (14–15) systemic velocity  $v_{\text{sys}}/v_{\text{sys},2}$ , (16–17) fractional kinematic offset from DEIMOS and SDSS  $\delta_x^{\text{vel}}/\delta_{x,2}^{\text{vel}}$ , (18–19) central brightness from DEIMOS and SDSS  $I_0^1/I_0^2$ , and (20) background  $bkg$ .

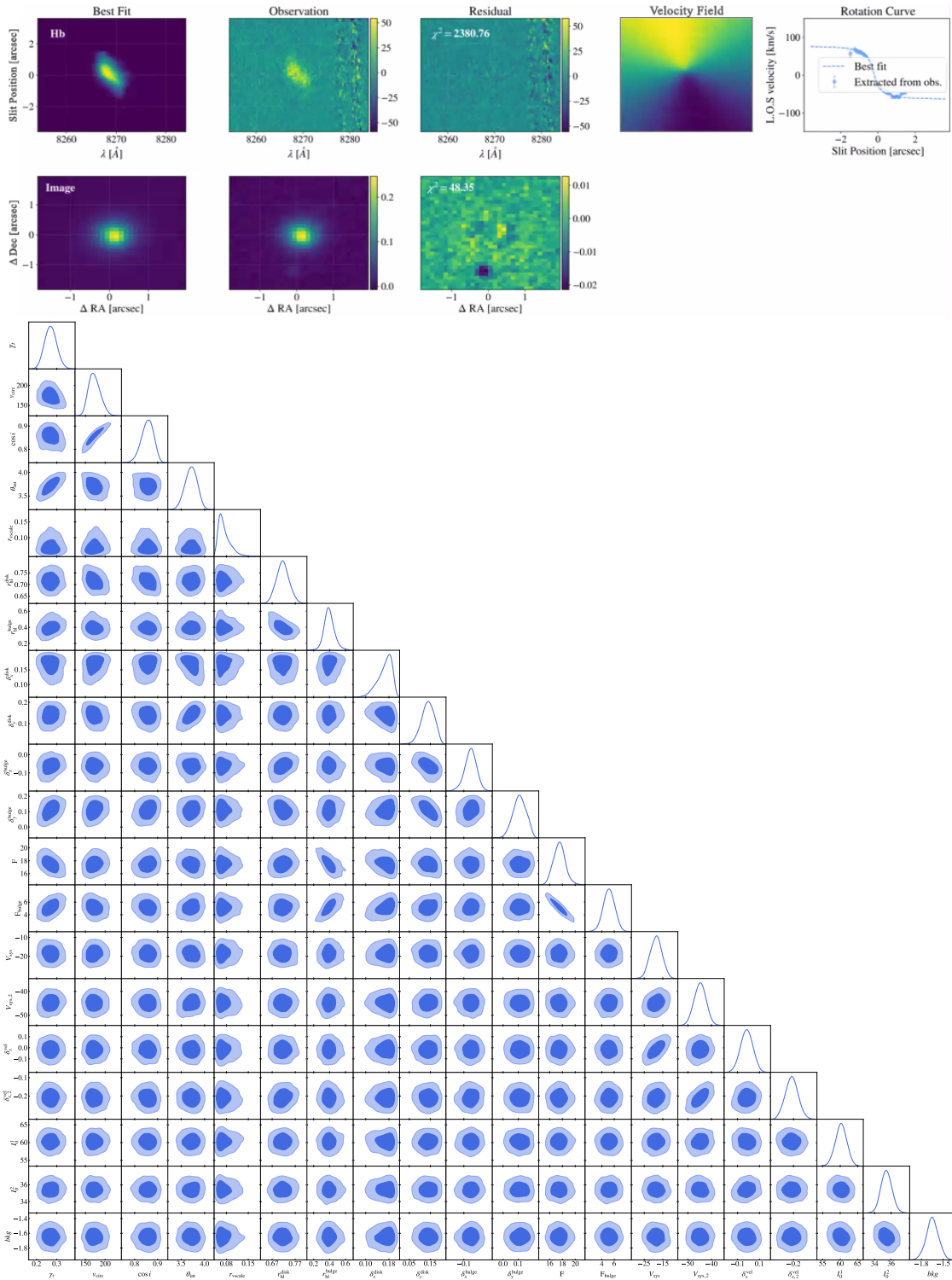


Figure 2.7: Rotation curve fit (*upper*) and posterior (*lower*) for Slit 19 (RA=260.69553°, Dec=32.08440°) of A2261 (Row 10 of Table 2.1). This figure is created and provided by Pranjal R. S.

Rotation curves are more important when it has redshifts greater than the cluster's redshifts. We say the background galaxies for those curves with redshifts 0.1 larger than the cluster's redshift, i.e.,  $z > z_{\text{Cl}} + 0.1$ . The numbers of rotation curves from all galaxies and background galaxies are listed in Table 2.1. In summary, the cluster sample comes up with 149 rotation curves where 105 curves belong to the background source galaxies.

Moreover, the rest of the rotation curves whose redshifts  $z \leq z_{\text{Cl}} - 0.1$  can be a key sample for training fittings since the galaxy is not weak-lensed yielding the observed shape from photometry is exactly the intrinsic shape, which the resultant  $\sin(i)$  from the rotation curve fitting will compare with.

## 2.4 Discussions and Future Works

### 2.4.1 Redshift Pipeline

This study proposes a batch process that combines the automated Python-based FIREFLY redshift guesses and IDL-based SPECPRO manual redshift measurements. The remaining 14 clusters and 40 masks in the cluster sample are being studied, but the processing time will be lengthy if the pipeline not be optimized.

It is important to improve FIREFLY so that most spectroscopic redshifts can be assessed automatically. Assuming the spectral feature of a slit of a target galaxy may be either absorption-type or emission-type, the best-fit spectroscopic redshift by FIREFLY would replace the manually-inspected confidence flag with a calculated cross-correlation parameter.

The current version of FIREFLY can fit the 1D spectrum with 2 templates, giving the cross-correlation values at redshift guesses (in Figure 2.8 *bottom panels*). A significant peak of the cross-correlation can be confident enough to represent the most likely spectroscopic redshift, while a sanity check of judging the galaxy type is also required. For example, Figure 2.8 has an emission-type spectrum with 2D as shown in the *top-left and top-right 1×2 panels* and 1D in black curves in the *lower 4×2 panels*. However, the cross-correlation peak at  $z = 0.0266$  for Template 1, an absorption-type template in all *left four panels*, is  $\sim 0.33$ , and about 3 times higher than at  $z = 0.0631$  for Template 2 on the *right*. FIREFLY is also able to identify the significant emission lines such as [O II] doublet as displayed in middle  $2 \times 2$  panels with a solution of  $z = 0.6209$ . This is expected and should be treated as the final secure redshift since the additional [O III] and H $\beta$  lines match well with the observed 1D spectrum, although it gives a lower correlation peak.

FIREFLY will be trained to achieve this expectation with a better consistency between manual visualization and quantitative judgment. Consequently, SPECPRO is expected as a supplement to

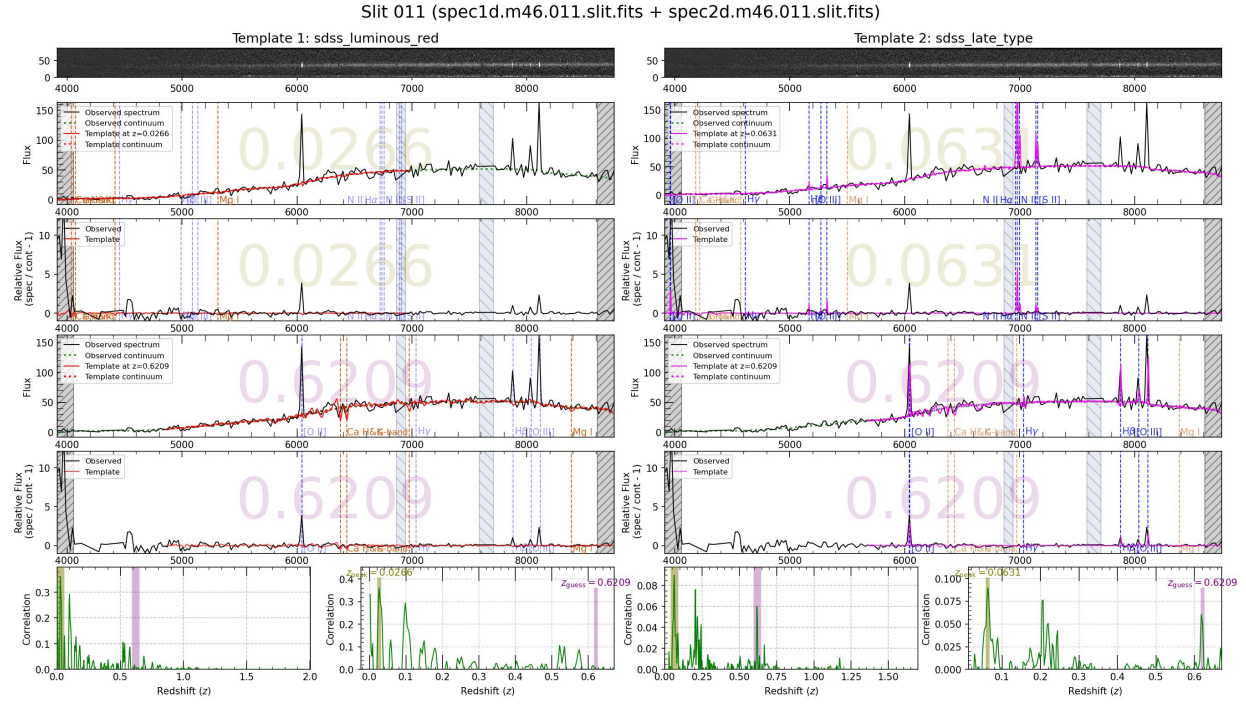


**Figure 2.8:** FIREFLY output for Slit 11 in A1758N. *Left* and *Right* columns are fittings for Template 1 (SDSS Luminous Red) and Template 2 (SDSS Late Type) respectively. *Top Row*: Two identical 2D spectra. *Second and Third Rows*: The fitting of the peak cross-correlation with the corresponding redshift guess  $z_{\text{peak}}$ . The vertical axes of the second and third rows are for flux and relative flux respectively. The FIREFLY fits the relative flux of the observed 1D spectrum and template. *Fourth and Fifth Rows*: Similar to the second and third rows but are forced to fit possible [O II] with resultant  $z_{\text{guess}}$ . *Bottom Row*: Cross-correlation distributions and zoom-ins around  $z_{\text{peak}}$  and  $z_{\text{guess}}$ .

handle a small number of unsecured redshifts and spectra for non-galaxy targets.

## 2.4.2 Shear Measurement

The fitting of rotation curves gives the magnitude and direction of the perpendicular shear component ( $\gamma_+$ ), which can be used to cross-check with the previous and current generation weak lensing surveys as stated in Section 1.2.2. These surveys may contain the cluster’s projected weak lensing mass map and the inferred shear depends on the mass density at the galaxy position.

## 2.4.3 Future MOS Instruments

The VLT/KMOS (Sharples et al. 2013), an integral-field MOS with  $14 \times 14$  fibers, is another powerful instrument in future research stages for its wavelength-calibration-free data assembled into data cubes of  $x$ -pixels,  $y$ -pixels, and spectroscopic  $\lambda$ -pixels (spaxels). This is convenient for di-

rectly mapping the velocity fields of up to 24 targets at one observation. There are 9 clusters with VLT/KMOS data archived and one cluster thereof, A370, has been selected in this paper. Therefore, VLT/KMOS will show its potential in future KL analysis.

#### 2.4.4 Discoveries of Active Galactic Nucleus

As inspecting the spectra of A2552, a few slits (e.g., Slit 68) show their emission line as two distinct bright dots separated for a few Å on the faint continuum. Slit 68 is an irregular spiral galaxy (WISEA J231142.18+033812.5) reported by NASA/IPAC Extragalactic Database<sup>9</sup>. This slit's target is then inferred as an active galactic nucleus or a system of distinct rotating black holes, which has not been studied in the literature.

### 2.5 Conclusions

This paper presented the archive-mining study on Keck/DEIMOS in a sample of *Weighing the Giants* project clusters. We reduced slit-spectroscopic data, discussed WL ideas, and showed rotation curves that can be fitted with resultant shears. The findings are as follows:

1. A total of 443 secure spectroscopic redshifts are measured and produced by 1125 slits in 6 sample clusters. This paper utilizes and develops multiple pipelines by combining automatic template fittings and redshift measurements.
2. We find 149 rotation curves that can solve for the weak lensing shear and reduce the shape noise. They are also valuable databases for future KL studies.

*This research is conducted by The Spectroscopy Team of A. von der Linden, J. Di, A. Beck, and A. Burke. Of the total research project's work, J. Di, A. Beck, and A. Burke contribute to Row 1–8, Row 9–17 of Table 2.1, and 6 masks to be published, respectively. The Spectroscopy Team has been organized since Spring 2023 and supervised by Anja von der Linden.*

---

<sup>9</sup><https://ned.ipac.caltech.edu/>

# Bibliography

Abazajian, K., Adelman-McCarthy, J. K., Agüeros, M. A., Allam, S. S., Anderson, K., Anderson, S. F., Annis, J., Bahcall, N. A., Baldry, I. K., Bastian, S., Berlind, A., Bernardi, M., Blanton, M. R., Bochanski, John J., J., Boroski, W. N., Briggs, J. W., Brinkmann, J., Brunner, R. J., Budavári, T., Carey, L. N., Carliles, S., Castander, F. J., Connolly, A. J., Csabai, I., Doi, M., Dong, F., Eisenstein, D. J., Evans, M. L., Fan, X., Finkbeiner, D. P., Friedman, S. D., Frieman, J. A., Fukugita, M., Gal, R. R., Gillespie, B., Glazebrook, K., Gray, J., Grebel, E. K., Gunn, J. E., Gurbani, V. K., Hall, P. B., Hamabe, M., Harris, F. H., Harris, H. C., Harvanek, M., Heckman, T. M., Hendry, J. S., Hennessy, G. S., Hindsley, R. B., Hogan, C. J., Hogg, D. W., Holmgren, D. J., Ichikawa, S.-i., Ichikawa, T., Ivezić, Ž., Jester, S., Johnston, D. E., Jorgensen, A. M., Kent, S. M., Kleinman, S. J., Knapp, G. R., Kniazev, A. Y., Kron, R. G., Krzesinski, J., Kunszt, P. Z., Kuropatkin, N., Lamb, D. Q., Lampeitl, H., Lee, B. C., Leger, R. F., Li, N., Lin, H., Loh, Y.-S., Long, D. C., Loveday, J., Lupton, R. H., Malik, T., Margon, B., Matsubara, T., McGehee, P. M., McKay, T. A., Meiksin, A., Munn, J. A., Nakajima, R., Nash, T., Neilsen, Eric H., J., Newberg, H. J., Newman, P. R., Nichol, R. C., Nicinski, T., Nieto-Santisteban, M., Nitta, A., Okamura, S., O'Mullane, W., Ostriker, J. P., Owen, R., Padmanabhan, N., Peoples, J., Pier, J. R., Pope, A. C., Quinn, T. R., Richards, G. T., Richmond, M. W., Rix, H.-W., Rockosi, C. M., Schlegel, D. J., Schneider, D. P., Scranton, R., Sekiguchi, M., Seljak, U., Sergey, G., Sesar, B., Sheldon, E., Shimasaku, K., Siegmund, W. A., Silvestri, N. M., Smith, J. A., Smolčić, V., Snedden, S. A., Stebbins, A., Stoughton, C., Strauss, M. A., SubbaRao, M., Szalay, A. S., Szapudi, I., Szkody, P., Szokoly, G. P., Tegmark, M., Teodoro, L., Thakar, A. R., Tremonti, C., Tucker, D. L., Uomoto, A., Vanden Berk, D. E., Vandenberg, J., Vogeley, M. S., Voges, W., Vogt, N. P., Walkowicz, L. M., Wang, S.-i., Weinberg, D. H., West, A. A., White, S. D. M., Wilhite, B. C., Xu, Y., Yanny, B., Yasuda, N., Yip, C.-W., Yocom, D. R., York, D. G., Zehavi, I., Zibetti, S. & Zucker, D. B. (2004), ‘The Second Data Release of the Sloan Digital Sky Survey’, *AJ* **128**(1), 502–512.

<https://doi.org/10.1086/421365>

Abell, G. O. (1958), ‘The Distribution of Rich Clusters of Galaxies.’, *ApJ Supplement* **3**, 211.  
<https://ui.adsabs.harvard.edu/abs/1958ApJS.....3..211A>

Aihara, H., Arimoto, N., Armstrong, R., Arnouts, S., Bahcall, N. A., Bickerton, S., Bosch, J., Bundy, K., Capak, P. L., Chan, J. H. H., Chiba, M., Coupon, J., Egami, E., Enoki, M., Finet, F., Fujimori, H., Fujimoto, S., Furusawa, H., Furusawa, J., Goto, T., Goulding, A., Greco, J. P.,

Greene, J. E., Gunn, J. E., Hamana, T., Harikane, Y., Hashimoto, Y., Hattori, T., Hayashi, M., Hayashi, Y., Hełminiak, K. G., Higuchi, R., Hikage, C., Ho, P. T. P., Hsieh, B.-C., Huang, K., Huang, S., Ikeda, H., Imanishi, M., Inoue, A. K., Iwasawa, K., Iwata, I., Jaelani, A. T., Jian, H.-Y., Kamata, Y., Karoji, H., Kashikawa, N., Katayama, N., Kawanomoto, S., Kayo, I., Koda, J., Koike, M., Kojima, T., Komiyama, Y., Konno, A., Koshida, S., Koyama, Y., Kusakabe, H., Leauthaud, A., Lee, C.-H., Lin, L., Lin, Y.-T., Lupton, R. H., Mandelbaum, R., Matsuoka, Y., Medezinski, E., Mineo, S., Miyama, S., Miyatake, H., Miyazaki, S., Momose, R., More, A., More, S., Moritani, Y., Moriya, T. J., Morokuma, T., Mukae, S., Murata, R., Murayama, H., Nagao, T., Nakata, F., Niida, M., Niikura, H., Nishizawa, A. J., Obuchi, Y., Oguri, M., Oishi, Y., Okabe, N., Okamoto, S., Okura, Y., Ono, Y., Onodera, M., Onoue, M., Osato, K., Ouchi, M., Price, P. A., Pyo, T.-S., Sako, M., Sawicki, M., Shibuya, T., Shimasaku, K., Shimono, A., Shirasaki, M., Silverman, J. D., Simet, M., Speagle, J., Spergel, D. N., Strauss, M. A., Sugahara, Y., Sugiyama, N., Suto, Y., Suyu, S. H., Suzuki, N., Tait, P. J., Takada, M., Takata, T., Tamura, N., Tanaka, M. M., Tanaka, M., Tanaka, M., Tanaka, Y., Terai, T., Terashima, Y., Toba, Y., Tominaga, N., Toshikawa, J., Turner, E. L., Uchida, T., Uchiyama, H., Umetsu, K., Uraguchi, F., Urata, Y., Usuda, T., Utsumi, Y., Wang, S.-Y., Wang, W.-H., Wong, K. C., Yabe, K., Yamada, Y., Yamanoi, H., Yasuda, N., Yeh, S., Yonehara, A. & Yuma, S. (2018), ‘The Hyper Suprime-Cam SSP Survey: Overview and survey design’, *PASJ* **70**, S4.

<https://doi.org/10.1093/pasj/psx066>

Allen, S. W., Evrard, A. E. & Mantz, A. B. (2011), ‘Cosmological Parameters from Observations of Galaxy Clusters’, *Annual Review of A&A* **49**(1), 409–470.

<https://doi.org/10.1146/annurev-astro-081710-102514>

Applegate, D. E., von der Linden, A., Kelly, P. L., Allen, M. T., Allen, S. W., Burchat, P. R., Burke, D. L., Ebeling, H., Mantz, A. & Morris, R. G. (2014), ‘Weighing the Giants - III. Methods and measurements of accurate galaxy cluster weak-lensing masses’, *MNRAS* **439**(1), 48–72.

<https://doi.org/10.1093/mnras/stt2129>

Bleem, L. E., Stalder, B., de Haan, T., Aird, K. A., Allen, S. W., Applegate, D. E., Ashby, M. L. N., Bautz, M., Bayliss, M., Benson, B. A., Bocquet, S., Brodwin, M., Carlstrom, J. E., Chang, C. L., Chiu, I., Cho, H. M., Clocchiatti, A., Crawford, T. M., Crites, A. T., Desai, S., Dietrich, J. P., Dobbs, M. A., Foley, R. J., Forman, W. R., George, E. M., Gladders, M. D., Gonzalez, A. H., Halverson, N. W., Hennig, C., Hoekstra, H., Holder, G. P., Holzapfel, W. L., Hrubes, J. D., Jones, C., Keisler, R., Knox, L., Lee, A. T., Leitch, E. M., Liu, J., Lueker, M., Luong-Van, D., Mantz, A., Marrone, D. P., McDonald, M., McMahon, J. J., Meyer, S. S., Mocanu, L., Mohr, J. J., Murray, S. S., Padin, S., Pryke, C., Reichardt, C. L., Rest, A., Ruel, J., Ruhl, J. E., Saliwanchik, B. R., Saro, A., Sayre, J. T., Schaffer, K. K., Schrabback, T., Shirokoff, E., Song, J., Spieler, H. G., Stanford, S. A., Staniszewski, Z., Stark, A. A., Story, K. T., Stubbs, C. W., Vanderlinde, K., Vieira, J. D., Vikhlinin, A., Williamson, R., Zahn, O. & Zenteno, A. (2015), ‘Galaxy Clusters Discovered via the Sunyaev-Zel’dovich Effect in the 2500-Square-Degree SPT-SZ Survey’, *ApJ Supplement* **216**(2), 27.

<https://doi.org/10.1088/0067-0049/216/2/27>

Böhringer, H., Schuecker, P., Guzzo, L., Collins, C. A., Voges, W., Cruddace, R. G., Ortiz-Gil, A., Chincarini, G., De Grandi, S., Edge, A. C., MacGillivray, H. T., Neumann, D. M., Schindler, S. & Shaver, P. (2004), ‘The ROSAT-ESO Flux Limited X-ray (REFLEX) Galaxy cluster survey. V. The cluster catalogue’, *A&A* **425**, 367–383.

<https://doi.org/10.1051/0004-6361:20034484>

Bolton, A., Abbott, T., Allen, L., Blanton, M., Bundy, K., Dawson, K., Dey, A., Kollmeier, J., Marshall, J., Moustakas, J., Najita, J., Newman, J. & Olsen, K. (2019), Towards a Spectroscopic Survey Roadmap for the 2020s and Beyond, in ‘Bulletin of the American Astronomical Society’, Vol. 51, p. 240.

<https://ui.adsabs.harvard.edu/abs/2019BAAS...51g.240B>

Carlstrom, J. E., Holder, G. P. & Reese, E. D. (2002), ‘Cosmology with the Sunyaev-Zel’dovich Effect’, *Annual Review of A&A* **40**, 643–680.

<https://doi.org/10.1146/annurev.astro.40.060401.093803>

Chang, C., Jarvis, M., Jain, B., Kahn, S. M., Kirkby, D., Connolly, A., Krughoff, S., Peng, E. H. & Peterson, J. R. (2013), ‘The effective number density of galaxies for weak lensing measurements in the LSST project’, *MNRAS* **434**(3), 2121–2135.

<https://doi.org/10.1093/mnras/stt1156>

Courteau, S. (1997), ‘Optical Rotation Curves and Linewidths for Tully-Fisher Applications’, *AJ* **114**, 2402.

<https://ui.adsabs.harvard.edu/abs/1997AJ....114.2402C>

Di, J., Egami, E., Wong, K. C., Lee, C.-H., Ning, Y., Ota, N. & Tanaka, M. (2023), ‘MMT/Binospec Spectroscopic Survey of Two  $z \sim 0.8$  Galaxy Clusters in the Eye of Horus Field’, *arXiv e-prints* p. arXiv:2312.02140.

<https://ui.adsabs.harvard.edu/abs/2023arXiv231202140D>

Diego, J. M., Meena, A. K., Adams, N. J., Broadhurst, T., Dai, L., Coe, D., Frye, B., Kelly, P., Koekemoer, A. M., Pascale, M., Willner, S. P., Zackrisson, E., Zitrin, A., Windhorst, R. A., Cohen, S. H., Jansen, R. A., Summers, J., Tompkins, S., Conselice, C. J., Driver, S. P., Yan, H., Grogin, N., Marshall, M. A., Pirzkal, N., Robotham, A., Ryan, R. E., Willmer, C. N. A., Bradley, L. D., Caminha, G., Caputi, K., Carleton, T. & Kamieneski, P. (2023), ‘JWST’s PEARLS: A new lens model for ACT-CL J0102–4915, “El Gordo,” and the first red supergiant star at cosmological distances discovered by JWST’, *A&A* **672**, A3.

<https://doi.org/10.1051/0004-6361/202245238>

Diego, J. M., Molnar, S. M., Cerny, C., Broadhurst, T., Windhorst, R., Zitrin, A., Bouwens, R., Coe, D., Conselice, C. & Sharon, K. (2020), ‘Free-form Lens Model and Mass Estimation of the High-redshift Galaxy Cluster ACT-CL J0102-4915, “El Gordo”’, *ApJ* **904**(2), 106.

<https://doi.org/10.3847/1538-4357/abbf56>

DiGiorgio, B., Bundy, K., Westfall, K. B., Leauthaud, A. & Stark, D. (2021), ‘A Novel Framework for Modeling Weakly Lensing Shear Using Kinematics and Imaging at Moderate Redshift’, *ApJ* **922**(2), 116.

<https://doi.org/10.3847/1538-4357/ac2572>

Ebeling, H., Barrett, E., Donovan, D., Ma, C. J., Edge, A. C. & van Speybroeck, L. (2007), ‘A Complete Sample of 12 Very X-Ray Luminous Galaxy Clusters at  $z \gtrsim 0.5$ ’, *ApJ* **661**(1), L33–L36.

<https://doi.org/10.1086/518603>

Ebeling, H., Edge, A. C., Allen, S. W., Crawford, C. S., Fabian, A. C. & Huchra, J. P. (2000), ‘The ROSAT Brightest Cluster Sample - IV. The extended sample’, *MNRAS* **318**(2), 333–340.

<https://doi.org/10.1046/j.1365-8711.2000.03549.x>

Ebeling, H., Edge, A. C., Bohringer, H., Allen, S. W., Crawford, C. S., Fabian, A. C., Voges, W. & Huchra, J. P. (1998), ‘The ROSAT Brightest Cluster Sample - I. The compilation of the sample and the cluster log N-log S distribution’, *MNRAS* **301**(4), 881–914.

<https://doi.org/10.1046/j.1365-8711.1998.01949.x>

Ebeling, H., Edge, A. C. & Henry, J. P. (2001), ‘MACS: A Quest for the Most Massive Galaxy Clusters in the Universe’, *ApJ* **553**(2), 668–676.

<https://doi.org/10.1086/320958>

Ebeling, H., Edge, A. C., Mantz, A., Barrett, E., Henry, J. P., Ma, C. J. & van Speybroeck, L. (2010), ‘The X-ray brightest clusters of galaxies from the Massive Cluster Survey’, *MNRAS* **407**(1), 83–93.

<https://doi.org/10.1111/j.1365-2966.2010.16920.x>

Eifler, T. (2015), ‘Mass Mapping Abell 2261 with Kinematic Weak Lensing: A Pilot Study for NASAs WFIRST mission’, Keck Observatory Archive DEIMOS, id.N177D.

<https://ui.adsabs.harvard.edu/abs/2015koa..prop..516E>

Eifler, T., Miyatake, H., Krause, E., Heinrich, C., Miranda, V., Hirata, C., Xu, J., Hemmati, S., Simet, M., Capak, P., Choi, A., Doré, O., Doux, C., Fang, X., Hounsell, R., Huff, E., Huang, H.-J., Jarvis, M., Kruk, J., Masters, D., Rozo, E., Scolnic, D., Spergel, D. N., Troxel, M., von der Linden, A., Wang, Y., Weinberg, D. H., Wenzl, L. & Wu, H.-Y. (2021), ‘Cosmology with the Roman Space Telescope - multiprobe strategies’, *MNRAS* **507**(2), 1746–1761.

<https://doi.org/10.1093/mnras/stab1762>

Faber, S. M., Phillips, A. C., Kibrick, R. I., Alcott, B., Allen, S. L., Burrous, J., Cantrall, T., Clarke, D., Coil, A. L., Cowley, D. J., Davis, M., Deich, W. T. S., Dietsch, K., Gilmore, D. K., Harper, C. A., Hilyard, D. F., Lewis, J. P., McVeigh, M., Newman, J., Osborne, J., Schiavon, R., Stover, R. J., Tucker, D., Wallace, V., Wei, M., Wirth, G. & Wright, C. A. (2003), The DEIMOS spectrograph for the Keck II Telescope: integration and testing, in M. Iye & A. F. M.

Moorwood, eds, ‘Instrument Design and Performance for Optical/Infrared Ground-based Telescopes’, Vol. 4841 of *Society of Photo-Optical Instrumentation Engineers (SPIE) Conference Series*, pp. 1657–1669.

<https://doi.org/10.1117/12.460346>

Fioc, M. & Rocca-Volmerange, B. (1997), ‘PEGASE: a UV to NIR spectral evolution model of galaxies. Application to the calibration of bright galaxy counts.’, *A&A* **326**, 950–962.

<https://ui.adsabs.harvard.edu/abs/1997A&A...326..950F>

Green, A. W., Glazebrook, K., McGregor, P. J., Damjanov, I., Wisnioski, E., Abraham, R. G., Colless, M., Sharp, R. G., Crain, R. A., Poole, G. B. & McCarthy, P. J. (2014), ‘DYNAMO - I. A sample of H $\alpha$ -luminous galaxies with resolved kinematics’, *MNRAS* **437**(2), 1070–1095.

<https://doi.org/10.1093/mnras/stt1882>

Gurri, P., Taylor, E. N. & Fluke, C. J. (2020), ‘The first shear measurements from precision weak lensing’, *MNRAS* **499**(4), 4591–4604.

<https://doi.org/10.1093/mnras/staa2893>

Gurri, P., Taylor, E. N. & Fluke, C. J. (2021), ‘Shape noise and dispersion in precision weak lensing’, *MNRAS* **502**(4), 5612–5621.

<https://doi.org/10.1093/mnras/stab423>

Hasselfield, M., Hilton, M., Marriage, T. A., Addison, G. E., Barrientos, L. F., Battaglia, N., Battistelli, E. S., Bond, J. R., Crichton, D., Das, S., Devlin, M. J., Dicker, S. R., Dunkley, J., Dünnér, R., Fowler, J. W., Gralla, M. B., Hajian, A., Halpern, M., Hincks, A. D., Hlozek, R., Hughes, J. P., Infante, L., Irwin, K. D., Kosowsky, A., Marsden, D., Menanteau, F., Moodley, K., Niemack, M. D., Nolta, M. R., Page, L. A., Partridge, B., Reese, E. D., Schmitt, B. L., Sehgal, N., Sherwin, B. D., Sievers, J., Sifón, C., Spergel, D. N., Staggs, S. T., Swetz, D. S., Switzer, E. R., Thornton, R., Trac, H. & Wollack, E. J. (2013), ‘The Atacama Cosmology Telescope: Sunyaev-Zel’dovich selected galaxy clusters at 148 GHz from three seasons of data’, *JCAP* **2013**(7), 008.

<https://doi.org/10.1088/1475-7516/2013/07/008>

Huff, E. M., Krause, E., Eifler, T., Fang, X., George, M. R. & Schlegel, D. (2013), ‘Cosmic shear without shape noise’, *arXiv e-prints* p. arXiv:1311.1489.

<https://doi.org/10.48550/arXiv.1311.1489>

Jee, M. J., Hughes, J. P., Menanteau, F., Sifón, C., Mandelbaum, R., Barrientos, L. F., Infante, L. & Ng, K. Y. (2014), ‘Weighing “El Gordo” with a Precision Scale: Hubble Space Telescope Weak-lensing Analysis of the Merging Galaxy Cluster ACT-CL J0102-4915 at z = 0.87’, *ApJ* **785**(1), 20.

<https://doi.org/10.1088/0004-637X/785/1/20>

Kelly, P. L., von der Linden, A., Applegate, D. E., Allen, M. T., Allen, S. W., Burchat, P. R., Burke, D. L., Ebeling, H., Capak, P., Czoske, O., Donovan, D., Mantz, A. & Morris, R. G.

(2014), ‘Weighing the Giants - II. Improved calibration of photometry from stellar colours and accurate photometric redshifts’, *MNRAS* **439**(1), 28–47.  
<https://doi.org/10.1093/mnras/stt1946>

Kilbinger, M. (2015), ‘Cosmology with cosmic shear observations: a review’, *Reports on Progress in Physics* **78**(8), 086901.  
<https://ui.adsabs.harvard.edu/abs/2015RPPPh...78h6901K>

Kravtsov, A. V. & Borgani, S. (2012), ‘Formation of Galaxy Clusters’, *Annual Review of A&A* **50**, 353–409.  
<https://doi.org/10.1146/annurev-astro-081811-125502>

Mandelbaum, R. (2018), ‘Weak Lensing for Precision Cosmology’, *Annual Review of A&A* **56**, 393–433.  
<https://doi.org/10.1146/annurev-astro-081817-051928>

Mantz, A., Allen, S. W., Ebeling, H., Rapetti, D. & Drlica-Wagner, A. (2010b), ‘The observed growth of massive galaxy clusters - II. X-ray scaling relations’, *MNRAS* **406**(3), 1773–1795.  
<https://doi.org/10.1111/j.1365-2966.2010.16993.x>

Mantz, A., Allen, S. W., Rapetti, D. & Ebeling, H. (2010a), ‘The observed growth of massive galaxy clusters - I. Statistical methods and cosmological constraints’, *MNRAS* **406**(3), 1759–1772.  
<https://doi.org/10.1111/j.1365-2966.2010.16992.x>

Masters, D. & Capak, P. (2011), ‘SpecPro: An Interactive IDL Program for Viewing and Analyzing Astronomical Spectra’, *PASP* **123**(903), 638–644.  
<http://iopscience.iop.org/article/10.1086/660023>

Oguri, M. (2014), ‘A cluster finding algorithm based on the multiband identification of red sequence galaxies’, *MNRAS* **444**(1), 147–161.  
<https://doi.org/10.1093/mnras/stu1446>

Oguri, M., Lin, Y.-T., Lin, S.-C., Nishizawa, A. J., More, A., More, S., Hsieh, B.-C., Medezinski, E., Miyatake, H., Jian, H.-Y., Lin, L., Takada, M., Okabe, N., Speagle, J. S., Coupon, J., Leauthaud, A., Lupton, R. H., Miyazaki, S., Price, P. A., Tanaka, M., Chiu, I. N., Komiyama, Y., Okura, Y., Tanaka, M. M. & Usuda, T. (2018), ‘An optically-selected cluster catalog at redshift 0.1  $\leq z \leq$  1.1 from the Hyper Suprime-Cam Subaru Strategic Program S16A data’, *PASJ* **70**, S20.  
<https://doi.org/10.1093/pasj/psx042>

Pickles, A. J. (1998), ‘A Stellar Spectral Flux Library: 1150–25000 Å’, *PASP* **110**(749), 863–878.  
<https://doi.org/10.1086/316197>

Pranjal, R. S., Krause, E., Huang, H.-J., Huff, E., Xu, J., Eifler, T. & Everett, S. (2023), ‘Kinematic lensing inference - I. Characterizing shape noise with simulated analyses’, *MNRAS*

**524**(3), 3324–3334.

<https://doi.org/10.1093/mnras/stad2014>

Prochaska, J., Hennawi, J., Westfall, K., Cooke, R., Wang, F., Hsyu, T., Davies, F., Farina, E. & Pelliccia, D. (2020), ‘PypeIt: The Python Spectroscopic Data Reduction Pipeline’, *The Journal of Open Source Software* **5**(56), 2308.

<https://ui.adsabs.harvard.edu/abs/2020JOSS....5.2308P>

Reichard, T. A., Richards, G. T., Schneider, D. P., Hall, P. B., Tolea, A., Krolik, J. H., Tsvetanov, Z., Vanden Berk, D. E., York, D. G., Knapp, G. R., Gunn, J. E. & Brinkmann, J. (2003), ‘A Catalog of Broad Absorption Line Quasars from the Sloan Digital Sky Survey Early Data Release’, *AJ* **125**(4), 1711–1728.

<https://doi.org/10.1086/368244>

Reichardt, C. L., Stalder, B., Bleem, L. E., Montroy, T. E., Aird, K. A., Andersson, K., Armstrong, R., Ashby, M. L. N., Bautz, M., Bayliss, M., Bazin, G., Benson, B. A., Brodwin, M., Carlstrom, J. E., Chang, C. L., Cho, H. M., Clocchiatti, A., Crawford, T. M., Crites, A. T., de Haan, T., Desai, S., Dobbs, M. A., Dudley, J. P., Foley, R. J., Forman, W. R., George, E. M., Gladadders, M. D., Gonzalez, A. H., Halverson, N. W., Harrington, N. L., High, F. W., Holder, G. P., Holzapfel, W. L., Hoover, S., Hrubes, J. D., Jones, C., Joy, M., Keisler, R., Knox, L., Lee, A. T., Leitch, E. M., Liu, J., Lueker, M., Luong-Van, D., Mantz, A., Marrone, D. P., McDonald, M., McMahon, J. J., Mehl, J., Meyer, S. S., Mocanu, L., Mohr, J. J., Murray, S. S., Natoli, T., Padin, S., Plagge, T., Pryke, C., Rest, A., Ruel, J., Ruhl, J. E., Saliwanchik, B. R., Saro, A., Sayre, J. T., Schaffer, K. K., Shaw, L., Shirokoff, E., Song, J., Spieler, H. G., Staniszewski, Z., Stark, A. A., Story, K., Stubbs, C. W., Suhada, R., van Engelen, A., Vanderlinde, K., Vieira, J. D., Vikhlinin, A., Williamson, R., Zahn, O. & Zenteno, A. (2013), ‘Galaxy Clusters Discovered via the Sunyaev-Zel’dovich Effect in the First 720 Square Degrees of the South Pole Telescope Survey’, *ApJ* **763**(2), 127.

<https://doi.org/10.1088/0004-637X/763/2/127>

Reyes, R., Mandelbaum, R., Gunn, J. E., Pizagno, J. & Lackner, C. N. (2011), ‘Calibrated Tully-Fisher relations for improved estimates of disc rotation velocities’, *MNRAS* **417**(3), 2347–2386.

<https://doi.org/10.1111/j.1365-2966.2011.19415.x>

Schneider, D. P., Richards, G. T., Hall, P. B., Strauss, M. A., Anderson, S. F., Boroson, T. A., Ross, N. P., Shen, Y., Brandt, W. N., Fan, X., Inada, N., Jester, S., Knapp, G. R., Krawczyk, C. M., Thakar, A. R., Vanden Berk, D. E., Voges, W., Yanny, B., York, D. G., Bahcall, N. A., Bizyaev, D., Blanton, M. R., Brewington, H., Brinkmann, J., Eisenstein, D., Frieman, J. A., Fukugita, M., Gray, J., Gunn, J. E., Hibon, P., Ivezić, Ž., Kent, S. M., Kron, R. G., Lee, M. G., Lupton, R. H., Malanushenko, E., Malanushenko, V., Oravetz, D., Pan, K., Pier, J. R., Price, Ted N., I., Saxe, D. H., Schlegel, D. J., Simmons, A., Snedden, S. A., SubbaRao, M. U., Szalay, A. S. & Weinberg, D. H. (2010), ‘The Sloan Digital Sky Survey Quasar Catalog. V. Seventh Data Release’, *AJ* **139**(6), 2360.

<https://doi.org/10.1088/0004-6256/139/6/2360>

- Seitz, C. & Schneider, P. (1997), ‘Steps towards nonlinear cluster inversion through gravitational distortions. III. Including a redshift distribution of the sources.’, *A&A* **318**, 687–699.  
<https://ui.adsabs.harvard.edu/abs/1997A&A...318..687S>
- Shapley, A. E., Steidel, C. C., Pettini, M. & Adelberger, K. L. (2003), ‘Rest-Frame Ultraviolet Spectra of z~3 Lyman Break Galaxies’, *ApJ* **588**(1), 65–89.  
<https://doi.org/10.1086/373922>
- Sharples, R., Bender, R., Agudo Berbel, A., Bezwada, N., Castillo, R., Cirasuolo, M., Davidson, G., Davies, R., Dubbeldam, M., Fairley, A., Finger, G., Förster Schreiber, N., Gonte, F., Hess, A., Jung, I., Lewis, I., Lizon, J. L., Muschielok, B., Pasquini, L., Pirard, J., Popovic, D., Ramsay, S., Rees, P., Richter, J., Riquelme, M., Rodrigues, M., Saviane, I., Schlichter, J., Schmidtobreick, L., Segovia, A., Smette, A., Szeifert, T., van Kesteren, A., Wegner, M. & Wiezorek, E. (2013), ‘First Light for the KMOS Multi-Object Integral-Field Spectrometer’, *The Messenger* **151**, 21–23.  
<https://ui.adsabs.harvard.edu/abs/2013Msngr.151...21S>
- Sunyaev, R. A. & Zeldovich, Y. B. (1972), ‘The Observations of Relic Radiation as a Test of the Nature of X-Ray Radiation from the Clusters of Galaxies’, *Comments on Astrophysics and Space Physics* **4**, 173.  
<https://ui.adsabs.harvard.edu/abs/1972CoASP...4..173S>
- Tanaka, M., Coupon, J., Hsieh, B.-C., Mineo, S., Nishizawa, A. J., Speagle, J., Furusawa, H., Miyazaki, S. & Murayama, H. (2018), ‘Photometric redshifts for Hyper Suprime-Cam Subaru Strategic Program Data Release 1’, *PASJ* **70**, S9.  
<https://doi.org/10.1093/pasj/psx077>
- Tully, R. B. & Fisher, J. R. (1977), ‘A new method of determining distances to galaxies.’, *A&A* **54**, 661–673.  
<https://ui.adsabs.harvard.edu/abs/1977A&A....54..661T>
- von der Linden, A., Allen, M. T., Applegate, D. E., Kelly, P. L., Allen, S. W., Ebeling, H., Burchat, P. R., Burke, D. L., Donovan, D., Morris, R. G., Blandford, R., Erben, T. & Mantz, A. (2014a), ‘Weighing the Giants - I. Weak-lensing masses for 51 massive galaxy clusters: project overview, data analysis methods and cluster images’, *MNRAS* **439**(1), 2–27.  
<https://doi.org/10.1093/mnras/stt1945>
- von der Linden, A., Mantz, A., Allen, S. W., Applegate, D. E., Kelly, P. L., Morris, R. G., Wright, A., Allen, M. T., Burchat, P. R., Burke, D. L., Donovan, D. & Ebeling, H. (2014b), ‘Robust weak-lensing mass calibration of Planck galaxy clusters’, *MNRAS* **443**(3), 1973–1978.  
<https://doi.org/10.1093/mnras/stu1423>
- Wang, T., Elbaz, D., Daddi, E., Finoguenov, A., Liu, D., Schreiber, C., Martín, S., Strazzullo, V., Valentino, F., van der Burg, R., Zanella, A., Ciesla, L., Gobat, R., Le Brun, A., Pannella, M.,

Sargent, M., Shu, X., Tan, Q., Cappelluti, N. & Li, Y. (2016), ‘Discovery of a Galaxy Cluster with a Violently Starbursting Core at  $z = 2.506$ ’, *ApJ* **828**(1), 56.  
<https://doi.org/10.3847/0004-637X/828/1/56>

Wittman, D. & Self, M. (2021), ‘Precision Weak Gravitational Lensing Using Velocity Fields: Fisher Matrix Analysis’, *ApJ* **908**(1), 34.  
<https://doi.org/10.3847/1538-4357/abd548>

Xu, J., Eifler, T., Huff, E., Pranjal, R. S., Huang, H.-J., Everett, S. & Krause, E. (2023), ‘Kinematic lensing with the Roman Space Telescope’, *MNRAS* **519**(2), 2535–2551.  
<https://doi.org/10.1093/mnras/stac3685>

Zwicky, F. (1933), ‘Die Rotverschiebung von extragalaktischen Nebeln’, *Helvetica Physica Acta* **6**, 110–127.  
<https://ui.adsabs.harvard.edu/abs/1933AcHPh...6..110Z>

Zwicky, F. (1937), ‘On the Masses of Nebulae and of Clusters of Nebulae’, *ApJ* **86**, 217.  
<https://doi.org/10.1086/143864>